# ATOMISTIC INVESTIGATIONS OF URANIUM

A Dissertation
Presented to
The Academic Faculty

by

Benjamin Warren Beeler

In Partial Fulfillment
of the Requirements for the Degree
Doctor of Philosophy in the
School of Mechanical Engineering

Georgia Institute of Technology
August 2013

# ATOMISTIC INVESTIGATIONS OF URANIUM

Approved by:

Dr. Chaitanya Deo, Advisor
School of Mechanical Engineering
*Georgia Institute of Technology*

Dr. Hamid Garmestani
School of Materials Science and Engineering
*Georgia Institute of Technology*

Dr. Mo Li
School of Materials Science and Engineering
*Georgia Institute of Technology*

Dr. Bojan Petrovic
School of Mechanical Engineering
*Georgia Institute of Technology*

Dr. Ting Zhu
School of Mechanical Engineering
*Georgia Institute of Technology*

Date Approved: 3/27/2013

## ACKNOWLEDGEMENTS

Thank you to my family and friends for their continued support.

# TABLE OF CONTENTS


| | | Page |
|---|---|---|
| ACKNOWLEDGEMENTS | | iii |
| LIST OF TABLES | | v |
| LIST OF FIGURES | | vi |
| SUMMARY | | vii |
| CHAPTER | | |
| 1 | Introduction | 1 |
| 2 | Computational Methods | 12 |
| | First Principles Calculations | 12 |
| | Molecular Statics and Dynamics Calculations | 17 |
| 3 | Bulk Properties and Intrinsic Defects of Uranium | 22 |
| | Properties of defect free γ-U | 22 |
| | Defect formation energies in γ-U | 25 |
| | Defect formation energies in α-U | 28 |
| 4 | Properties of Extrinsic Defects in Uranium | 31 |
| | Dilute Zr defect formation energies in γ-U | 31 |
| | Fission gas defect formation energies and incorporation energies in γ-U | 33 |
| | Fission gas defect formation energies and incorporation energies in α-U | 38 |
| 5 | MEAM Interatomic Potential for γ Uranium | 42 |
| | Molecular Statics Simulations | 42 |
| | Molecular Dynamics Simulations | 47 |
| 6 | Binary MEAM Interatomic Potentials for γ U-Xe, U-Kr and U-He | 55 |
| | Molecular Statics Calculations | 55 |

Molecular Dynamics Simulations 61

7 Conclusions 88

8 Appendix A: Discussion 90

9 Appendix B: Software Packages 91

REFERENCES 92

# LIST OF TABLES

Page

Table 1: Parameters of the MEAM potential for γ U, the value of the parameters. 21

Table 2: The properties of defect free b.c.c U. 24

Table 3: The formation energy of vacancies in bcc U. 25

Table 4: The lattice parameters (a, b, c and y), volume per atom and the vacancy formation energy calculated for the orthorhombic α allotrope of uranium. 29

Table 5: Formation energy (eV) of self-defects in orthorhombic α uranium. 30

Table 6: Formation energies (eV) of He, Xe and Kr in bcc uranium. 33

Table 7: Incorporation energies (eV) of He, Xe and Kr in bcc uranium. 35

Table 8: Formation energies (eV) of He, Xe and Kr in orthorhombic uranium. 38

Table 9: Incorporation energies (eV) of He, Xe and Kr in orthorhombic uranium. 39

Table 10. The equilibrium lattice constant at 0 K and the volume per atom at 0 K. 43

Table 11. Elastic constants for γ uranium at 0 K. 44

Table 12. The melting temperature, enthalpy of fusion, volume change on melting, specific heat capacity and thermal expansion are calculated and compared to experimental values. 53

Table 13. Equilibrium lattice parameters and formation energies for U-Xe, U-Kr and U-He theoretical intermetallic phases calculated with first principles DFT methods. 56

Table 14. MEAM parameters for a bcc uranium-fission gas potential. 57

Table 15. Formation energies (eV) of helium point defects in bcc uranium calculated via density functional theory and using a MEAM potential. 58

Table 16. Formation energies (eV) of xenon point defects in bcc uranium calculated via density functional theory and using a MEAM potential. 58

Table 17. Formation energies (eV) of krypton point defects in bcc uranium calculated via density functional theory and using a MEAM potential. 58

# LIST OF FIGURES

Page

Figure 1. The phase diagram of the uranium-zirconium binary system. 2

Figure 2. The α-U crystal structure. 3

Figure 3. The β-U crystal structure. 4

Figure 4. The γ-U crystal structure. 4

Figure 5: Schematic of the geometry used for calculating the formation energy of a <100> oriented dumbbell interstitial for a supercell with 129 atoms. 16

Figure 6: The total energy of the perfect bcc uranium lattice as a function of the supercell lattice parameter (PBE). 23

Figure 7: The total energy of the perfect bcc uranium lattice as a function of the supercell lattice parameter (PW91). 23

Figure 8: Self-defect formation energies calculated using the PBE exchange-correlation functional and a k-point mesh of 4x4x4. 27

Figure 9: Schematic of the face-centered orthorhombic crystal structure of α-U. 28

Figure 10: The free space defect in α-U. 29

Figure 11: Schematic of split dumbbell interstitials in α-U. 30

Figure 12: Zr defect formation energies calculated using the PBE functional and a k-point mesh of 4x4x4. 32

Figure 13: Formation energies (eV) of He, Xe and Kr in bcc uranium. 34

Figure 14: Incorporation energies (eV) of He, Xe and Kr in bcc uranium 35

Figure 15: Formation energies (eV) of He, Xe and Kr in orthorhombic uranium 39

Figure 16: Incorporation energies (eV) of He, Xe and Kr in orthorhombic uranium 40

Figure 17. Shear constant of γ U as a function of hydrostatic pressure at 0 K. 45

Figure 18. Vacancy formation energy versus hydrostatic pressure. 46

Figure 19. Cohesive energy of γ and liquid uranium in the temperature range 800-2000 K 49

Figure 20. The γ-liquid interface, the γ phase at 1400 K and the liquid structure at 1420 K 50

Figure 21. The equilibrium volume per atom as a function of temperature. 52

Figure 22. The vacancy formation energy in γ U as a function of temperature. 53

Figure 23. The self-interstitial formation energy in γ U as a function of temperature. 54

Figure 24. Formation energies (eV) of helium point defects in bcc uranium calculated via density functional theory and using a MEAM potential. 58

Figure 25. Formation energies (eV) of xenon point defects in bcc uranium calculated via density functional theory and using a MEAM potential. 59

Figure 26. Formation energies (eV) of krypton point defects in bcc uranium calculated via density functional theory and using a MEAM potential. 60

Figure 27. Formation energy of a multiple vacancy systems as a function of the number of vacancies within that system at 800 K. 63

Figure 28. Formation energy of a multiple vacancy systems as a function of the number of vacancies within that system from 800 K to 1200 K. 64

Figure 29. Swelling percent as a function of the number of vacancies comprising a single void at 800 K. 66

Figure 30. Xenon substitutional formation energy as a function of temperature. 67

Figure 31. Formation energy of a xenon bubble as a function of the number of xenon atoms present within the bubble 68

Figure 32. Bubble volume as a function of the number of Xe atoms within the bubble. 69

Figure 33. The maximum number of xenon atoms that can be inserted in a void of a given size without the creation of a self-interstitial atom. 70

Figure 34. The energy difference of nearest neighbor configurations of a vacancy and a Xe substitutional with respect to defects isolated in the bulk. 72

Figure 35. Mean squared displacement of monovacancy systems as a function of time at 800 K. 74

Figure 36. Mean squared displacement of monovacancy systems as a function of time at 900 K. 75

Figure 37. Mean squared displacement of monovacancy systems as a function of time at 1100 K. 76

Figure 38. Mean squared displacement of monovacancy systems as a function of time at 1300 K. 77

Figure 39. Mean squared displacement of four vacancy systems as a function of time at 800 K. 79

Figure 40. Mean squared displacement of four vacancy systems as a function of time at 900 K. 80

Figure 41. Mean squared displacement of four vacancy systems as a function of time at 1100 K. 81

Figure 42. Mean squared displacement of four vacancy systems as a function of time at 1300 K. 82

Figure 43. Effective diffusion coefficient as a function of temperature. 85

Figure 44. Effective diffusion coefficient of four vacancy systems as a function of temperature. 86

# SUMMARY

Uranium (U) exhibits a high temperature body-centered cubic (bcc) allotrope that is often stabilized by alloying with transition metals such as Zr, Mo, and Nb for technological applications. One such application involves U–Zr as nuclear fuel, where radiation damage and diffusion (processes heavily dependent on point defects) are of vital importance. Metallic nuclear fuels swell under fission conditions, creating fission product gases such as helium, xenon and krypton. Several systems of U are examined within a density functional theory framework utilizing projector augmented wave pseudopotentials. The bulk modulus, the lattice constant, and the Birch–Murnaghan equation of state for the defect free bcc uranium allotrope are calculated. Defect parameters calculated include energies of formation of vacancies in the α and γ allotropes, as well as self-interstitials, Zr, He, Xe and Kr interstitial and substitutional defects. This work is utilized in the construction of modified Embedded-Atom Method interatomic potentials for the bcc phase of uranium as well as the binary systems of U-Xe, U-Kr and U-He. Using this potential, equilibrium volume and elastic constants are calculated at 0 K and found to be in close agreement with previous first principles calculations. Further, the melting point, heat capacity, enthalpy of fusion, thermal expansion and volume change upon melting are calculated and found to be in reasonable agreement with experiment. Calculations of dilute fission gas defects show reasonable agreement with first principles calculations. Finally, void and xenon bubble energetics are analyzed as a function of temperature.

# CHAPTER 1

# INTRODUCTION

Metal alloy fuels have a long history in fast-reactor applications dating back to the earliest days of reactor development at the Metallurgical Laboratory of the University of Chicago [1-3]. Metallic fuel cores were employed in the sodium-potassium eutectic-cooled Experimental Breeder Reactor I (EBR-I), the world's first experimental fast neutron breeder reactor, between 1951 and 1963. Its successor, the sodium-cooled Experimental Breeder Reactor II (EBR-II), was also powered by a number of metallic fuel cores during its operation from 1964 until 1992. The EBR-II was used to study the performance of a variety of experimental metal alloy fuels in addition to a myriad of other fuel types, including oxides and nitrides. Other fast reactors that have utilized metallic fuel cores include the Fermi reactor in the United States and the Dounreay reactor in the United Kingdom.

Metal alloy fuels have demonstrated superior performance in that they behave in a benign manner during core off-normal events, maintain integrity to high burnup, and lend themselves to low-loss recycling processes as well as ease of operation and low minor actinide (MA) fabrication loss under remote-handling conditions [4]. However, most of the fundamental properties and behavior of these materials have not been measured and are not well understood.

Some of the metallic fuel types used or tested in fast spectrum reactors were high-enriched uranium (HEU), Pu-Al alloys, U-Mo alloys, U-Pu-Zr alloys, and U-fissium and U-Pu-fissium alloys (fissium is a mixture of Zr, Nb, Mo, Ru, Rh, and Pd). In addition, many small thermal spectrum research and test reactors employ metallic fuel such as U-

Mo alloys in Al cladding or dispersion fuel of U-Mo alloy in Al matrix. Recent efforts to develop metal alloy fuels for actinide transmutation in either fast-flux reactors or accelerator-driven systems of a closed nuclear fuel cycle have included studies on U-Pu-MA-Zr and Pu-MA-Zr (MA = minor actinides = Np, Am, Cm) alloys. Most of these contain uranium as the base element with varying alloying additions. The alloying additions attempt to stabilize the high temperature body-centered cubic (bcc gamma) phase at the expense of the anisotropic face-centered orthorhombic (alpha) phase. However, spent metallic fuels usually take the orthorhombic form. The phase diagram of U-Zr is shown in Figure 1 [5].

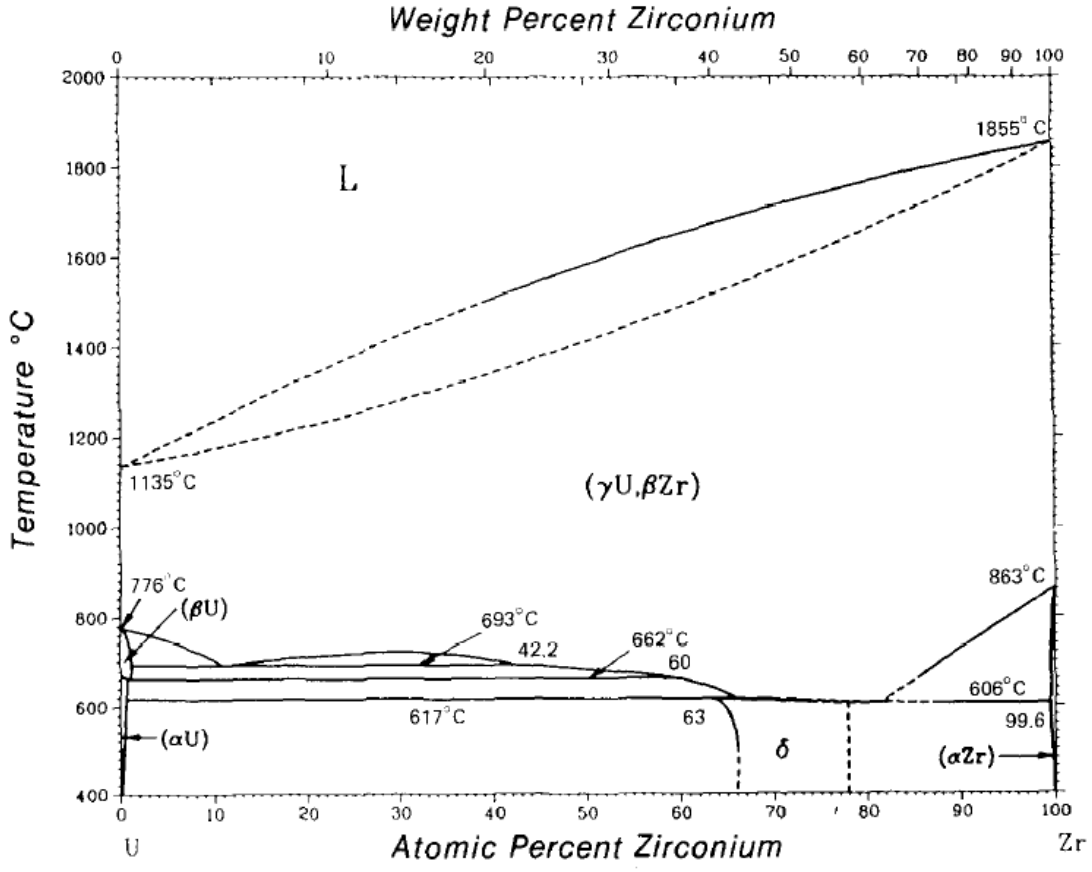


Figure 1. The phase diagram of the uranium-zirconium binary system.

One issue encountered with metallic U alloy fuels is swelling. The dramatic swelling of metallic fuels under irradiation is largely due to the incorporation of fission product gases in the fuel matrix during burnup. The specific isotopic yields for fission products (FP) vary based on fuel composition and the type of reactor. Three common gases present in the fission environment are helium, xenon and krypton. Research efforts [6] in the past have focused on understanding and predicting the constituent redistribution in metallic alloy fuels as this is of importance to the overall interpretation of fuel element behavior. However, unlike $UO_2$ commercial fuels, reliable experimental data on defect energies that impact fuel performance during its operation and subsequent long term storage are very scarce.

Uranium, an actinide exhibiting delocalized f-electrons, exists in three solid allotropes: α (face-centered orthorhombic), β (body-centered tetragonal) and γ (body-centered cubic)[7]. At elevated temperatures, uranium transforms from α to β at approximately 935 K and β transforms to γ at approximately 1045 K [8]. The α, β and γ crystal structures are shown respectively in figures 2-4.

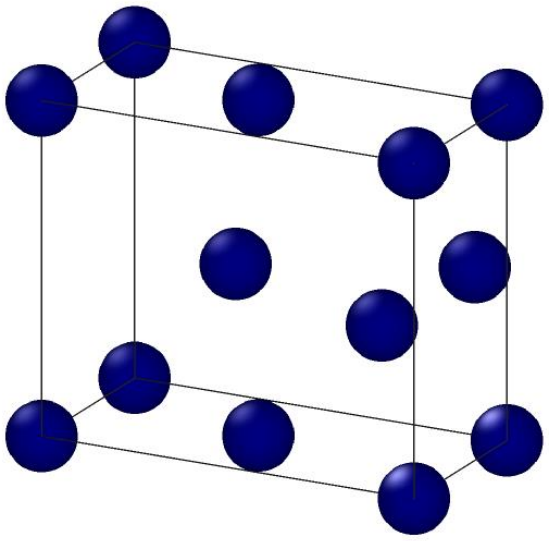

Figure 2. The α-U crystal structure.

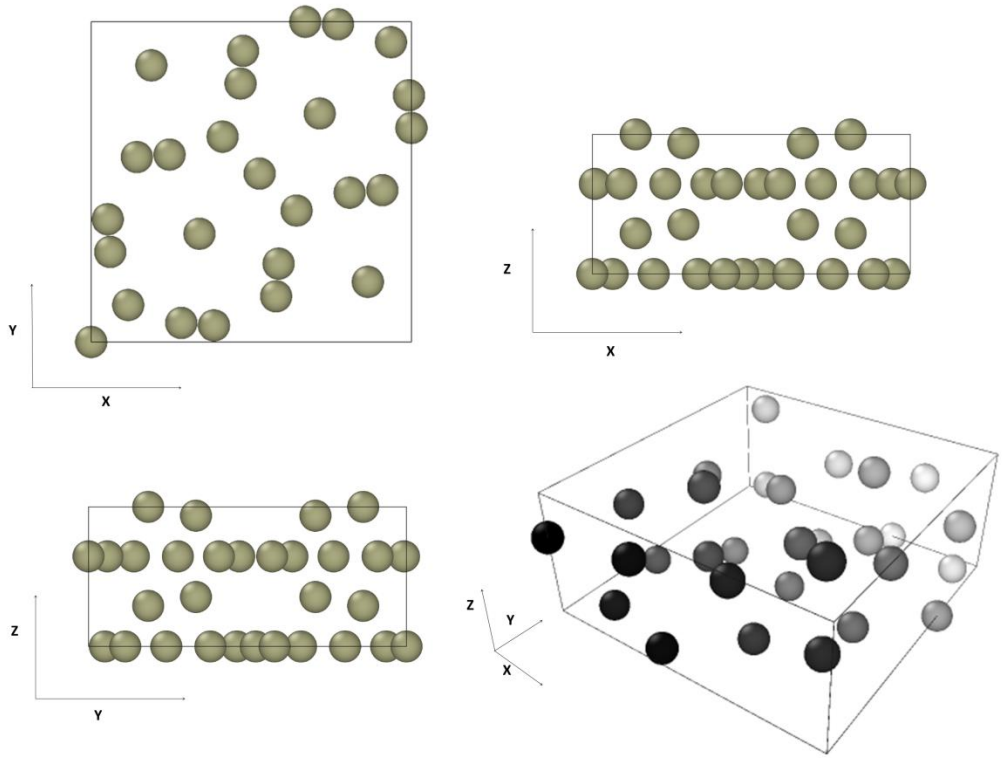


Figure 3. The β-U crystal structure.

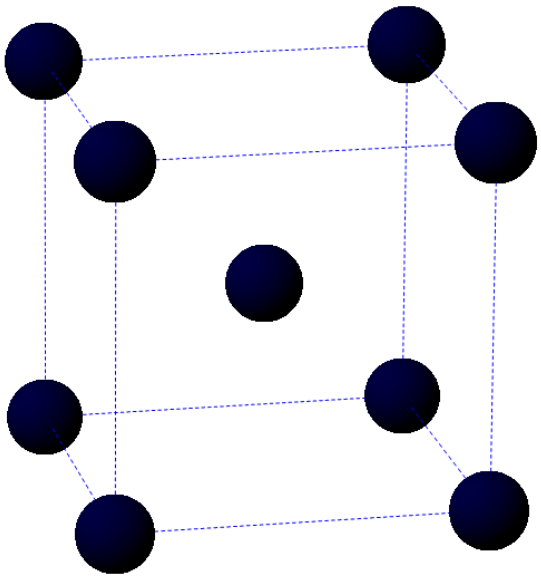

Figure 4. The γ-U crystal structure.

Detailed knowledge of fundamental processes occurring within these fuels is required for the development of understanding of the overall macroscopic processes. The goal of computational fuel research is eventually the development of a predictive continuum level software package that incorporates physics and physical processes occurring on atomistic and microscopic levels. Experimental data is also incorporated as input parameters. However, the experimental database is limited and further experimental investigations in these systems are inherently limited in scope. Computational modeling allows for the investigation of systems beyond the reach of experimental tools, exploring atomistic and microscopic properties occurring on minute time and length scales. Utilization of various computational tools on various time and length scales is required for the advancement of the total research database on alloy fuels. Studies such as this add to the limited framework of computational investigations into uranium and uranium based alloys. A brief summary of such previous computational studies is presented below.

Several examinations of U via a first principles methodology have been performed on the orthorhombic and body-centered cubic structures of U. Soderlind [9] implemented a full-potential linear muffin-tin orbital (FPLMTO) method to calculate lattice and elastic constants of α-U. Lattice constants were predicted within 1% of experimental values [10], while the bulk modulus was slightly overestimated when compared to experiment [8]. Crocombette et al. [11] utilized a norm-conserving pseudopotential method with a very high cutoff energy (2448 eV), resulting in a greater variance of lattice parameters and a greater overestimation of the bulk modulus. Taylor [12] used a projector-augmented wave (PAW) pseudopotential developed for U by

Kresse and Fürthmuller [13] with a cutoff energy of 253 eV to calculate the lattice constants of α-U and γ-U along with the bulk modulus of both allotropes. Taylor [12] also calculated the vacancy formation energy in the α allotrope. The lattice and elastic constants are predicted with comparable accuracy to the full-potential methods in the α allotrope, but the bulk modulus of the γ allotrope is significantly overestimated when compared with experiment [7]. An analysis of bulk properties in the α and γ allotropes, as well as an analysis of defects in γ-U, was performed by Xiang et al.[14] utilizing a PAW pseudopotential. Lattice and elastic constants for α-U and γ-U correspond with experimental values [7, 10] and the vacancy formation energy is slightly underestimated with respect to vacancy formation energies estimated through positron annihilation spectroscopy [15]. Recently, PAW pseudopotential calculations have been performed analyzing defects in α-U [16].

From the preceding literature review, only two studies have attempted to calculate point defect properties in U; these have been calculations focused on the vacancy formation energy in the α [12, 16] and the γ [14] allotropes. The explanation for such a limited scope of analysis on the defects lies partially in the inherent issues associated with a density functional theory (DFT) approach to the study of a high temperature allotrope and partially in computational limitations.

Density functional calculations are typically performed to calculate ground state properties, implying that the calculation is taking place at a temperature equal to 0 K. It has been shown, via the calculation of elastic constants, that the elastic shear constant ($C' = (C_{11} - C_{12})/2$) is negative in the body-centered cubic allotrope of U at 0 K [8]. Thus, at low temperatures, bcc U is mechanically unstable. Computationally, this mechanical

instability translates into an inability to calculate relaxed structures involving defects, due to the inherent localized deformation created by introducing a point defect. Several other systems, such as Zr, Ti, and Hf, also exhibit a high temperature body-centered cubic allotrope that is mechanically unstable at low temperature [17, 18].

Another issue relates to the size of the supercell studied. If a small supercell is analyzed, there can be cross-boundary effects due to the inherent periodicity of the supercell, creating defect–defect interactions, and thus a different system than the intent of the study. Boundary effects have been witnessed in bcc supercells as large as 54 atoms, and since typical plane wave calculations scale as $N^3$ (where N is the number of valence electrons), the computational expense increases dramatically for larger systems. In addition, the core of the U pseudopotential is large, potentially leading to large overlap of the cores as atoms move in response to defect strain fields in certain systems. The response may be to discard pseudopotential methods in favor of more accurate techniques. However, the use of more accurate methods (FP-LMTO, etc.[19]) leads to a limitation on system size through very high computational expense, thus limiting applicable first principles methodologies to pseudopotential based density functional theory calculations for the investigation of defect properties.

Analysis of defect properties at 0 K can provide excellent insight into defect mechanisms; however, ground state properties cannot always be extrapolated to high temperature. Unlike most first principles calculations, interatomic potentials based on mostly classical descriptions can be used to calculate relevant atomistic properties at temperature. Very few properties of the γ phase have been calculated due to its propensity to destabilize at 0 K. Thus, in order to understand the properties of this phase,

it is important to evaluate it when it is stable, i.e., at high temperature. Such calculations are inaccessible to most first principles methods, however semi-empirical interatomic potentials can be fit to both first principles and experimental data and employed to simulate high temperature properties.

Unlike first principles calculations, in classical simulations atoms are represented by point-like centers, which interact through many-body interactions defined by a set of equations - the interatomic potential. In this manner, the highly complex description of electron dynamics is replaced by an effective model whose main features such as the hard core of particles and internal degrees of freedom are described by a set of parameters and analytical functions, which depend on the mutual positions of the atoms in the configuration. These parameters and functions give complete information about the system energy, as well as about the forces acting on each particle.

The best choice of a potential for simulations of metals is a many-body potential. Pair-wise potentials, such as the Lennard - Jones (LJ) [20] potentials do not give adequate description of all the properties of metals. For example, the LJ potential imposes the Cauchy relation $C_{12} = C_{44}$ on the elastic constants. For the $\gamma$ phase of uranium, such constraints would give incorrect properties as the structure is mechanically unstable at 0 K implying a negative shear elastic constant. Pair-wise potentials fail to estimate the structure relaxation and reconstruction around point defects (vacancies and self-interstitials) in metals. The vacancy formation energy obtained by means of pair - wise potentials is overestimated, and is found to be about equal to the bulk cohesive energy [20].

A many-body potential includes pair-wise interactions as one component of the full potential. This first component of the many-body potential accounts for the core - core interactions (or ion - ion interactions), while the second part incorporates the complex nature of metallic cohesion by an additional term-the embedding function-that depends on electronic charge density. This is shown in equation 1:

$$E = \frac{1}{2}\sum_{i,i\neq j}^{N} \Phi\left(\mathrm{r_{ij}}\right) + \sum_{\mathrm{i=1}}^{\mathrm{N}} \mathrm{F}(\zeta_{\mathrm{i}}) \qquad (1)$$

where $\Phi\left(\mathrm{r_{ij}}\right)$ is the pair (two body) interaction and the many body term $\mathrm{F}(\zeta_{\mathrm{i}})$ depends on the electronic charge density $\zeta_{\mathrm{i}}$ around the atom i.

Very few interatomic potentials for actinide metals have been developed. Itinerant f-electron behavior has proved difficult to describe. Directional effects of the electron cloud need to be considered in the potential description. Of the actinide metals, interatomic descriptions of plutonium atomic interactions are available [21] and are based on the modified Embedded-Atom Method [22]. These potentials have been used to calculate the stability of Pu phases, the phase diagrams of Pu alloys, defect properties and radiation damage effects [23-26]

Very limited interatomic potential development has been undertaken on uranium and consequently its alloys. This neglect is mainly due to its inherent complexity shared with other actinides such as Pu. A recent attempt at an embedded atom method has been reported wherein the thermophysical properties of liquid uranium have been calculated [27] whose EAM based potential produces good agreement with experiment as regards the structure, density, and potential energy of liquid metal at temperatures up to 5000 K,

but is not intended for describing crystalline uranium properties. Two other recent publications[28, 29] report potentials suitable for investigating crystalline uranium in the α phase, however, no such potential exists that provides satisfactory results for the γ phase of U.

In this work, a detailed study of defect formation in α and γ uranium using pseudopotential based DFT calculations is performed. First, the equilibrium lattice constants and the bulk modulus are calculated in both U allotropes. The vacancy formation energy in the orthorhombic α allotrope and the γ allotrope is calculated. Several systems involving self-interstitials in α-U and γ-U are investigated for the computation of interstitial formation energies. Body-centered cubic systems of U are considered with a dilute concentration of Zr in the form of substitutional and interstitial atoms, calculating the formation energies of these defects. Formation and incorporation energies of Xe, Kr, and He for various defect positions are investigated for the prediction of fission product behavior. Where mechanical instabilities occur, an approximation technique is employed to calculate defect properties. A semi-empirical modified Embedded-Atom Method (MEAM) potential is presented for the description of the high temperature body-centered cubic phase of uranium. Atomistic simulations are performed for the calculation of equilibrium and thermodynamic properties. These include the melting point, heat capacity, enthalpy of fusion, thermal expansion and volume change on melting. Defect energies are analyzed as a function of pressure and temperature. This MEAM interatomic potential is utilized for the generation of binary interatomic potentials to characterize systems of bcc uranium with inclusions of Xe, Kr and He. Molecular statics is used to analyze He, Xe and Kr defects in bcc uranium at 0 K and

compare with DFT results. Finally, voids, xenon dilute defects and xenon bubbles are investigated as a function of temperature.

# CHAPTER 2

# COMPUTATIONAL METHODS

## First Principles Calculations

Calculations were performed using the Vienna *ab initio* Simulation Package (VASP) [13, 30, 31]. The Projector-Augmented Wave method [32] is utilized within the density functional theory [33, 34] framework. Calculations are performed using the Perdew-Burke-Ernzerhof (PBE) [35] and the Perdew-Wang (PW91) [36] GGA density functional implementation for the description of the exchange-correlation. Methfessel and Paxton's smearing method [37] of the first order is used with a width of 0.2 eV to determine the partial occupancies for each wave function. Structural relaxations are performed using the conjugate gradient method until a convergence of 1 meV is reached for the total energy of the system. A uranium PAW pseudopotential with the $6s^2 6p^6 5f^3 6d^1 7s^2$ valence electronic configuration and a [Xe, 5d, 4f] core is utilized. Fission product PAW pseudopotentials (PP) used include a helium PP with the valence of $1s^2$, a xenon PP with the valence of $5s^2 5p^6$ and a [Kr, 4d10] core, and a krypton PP with the valence of $4s^2 4p^6$ and a [Ar, 3d10] core. The cutoff energy is 253 eV for the U-Xe and U-Kr systems and 479 eV for the U-He system.

The structural relaxation for the γ phase was performed on a 128 atom supercell (4x4x4) to find equilibrium lattice constants. For the α phase, a 96 atom supercell (4x2x3) was fully relaxed to calculate bulk equilibrium properties. In both systems, symmetry restrictions were removed, resulting in 36 k-points in the irreducible wedge of the Brillouin Zone (BZ). These calculations were performed for various k-point meshes, and the variance is less than 0.05 eV for a more dense mesh. Boundary effects have been

observed in bcc supercells as large as 54 atoms, so supercells in this study were sufficiently large to minimize cross boundary effects relating to the inherent periodicity of the system, while still remaining computationally feasible.

Defects were introduced into a supercell with equilibrium lattice constants and a structural relaxation of atomic positions was performed to calculate the formation energies. In the calculation of defect formation energies, only isolated, non-interacting defects were considered, and the energy of an isolated atom in a vacuum at its ground state is assumed to be zero, providing the reference point for the calculations [14]. The formation energy of a single vacancy is defined as

$$E_v = E_{(n-1)U} - \left[\frac{n-1}{n}\right] E_{nU} \quad (2)$$

where $E_{(n-1)U}$ is the total energy of an (n−1)U atom supercell containing one uranium vacancy, and $E_{nU}$ is the total energy of an ideal uranium supercell containing n lattice sites. The formation energy of a U interstitial is defined as

$$E_i = E_{(n+1)U} - \left[\frac{n+1}{n}\right] E_{nU} \quad (3)$$

where $E_{(n+1)U}$ is the total energy of (n + 1)U atoms, which includes the atoms at lattice positions as well as one interstitial. The formation energy of a Zr substitutional is defined as

$$E_s = E_{(n-1)U+Zr} - \left[\frac{n-1}{n}\right] E_{nU} - E_{Zr} \quad (4)$$

where $E_{(n-1)U+Zr}$ is the energy of a lattice containing one Zr substitutional and $E_{Zr}$ is the energy of one Zr atom in the bcc allotrope. The formation energy of a Zr interstitial is defined as

$$E_i = E_{nU+Zr} - E_{nU} - E_{Zr} \quad (5)$$

where $E_{nU+Zr}$ is the energy of a lattice containing one Zr interstitial.

The reference state for the fission gases was assumed to be an equilibrium face-centered cubic structure (fcc). The fcc crystal structure was chosen as the reference state due to the fact that these calculations are occurring at 0 K, and as these systems approach 0 K, they will crystallize. The ground state crystal structure for Xe and Kr is a face-centered cubic lattice. The ground state crystal structure for He is the hexagonal close-packed (hcp) lattice. However, in order to keep a consistent reference state for all incorporated external atoms, fcc He is chosen as the ground state. The variance between the hcp and the fcc structures for He is less than 0.01 eV. The formation energy of a single substitutional defect is defined as

$$E_s = E_{(n-1)U+FG} - \left[\frac{n-1}{n}\right] E_{nU} - E_{FG} \quad (6)$$

where $E_{(n-1)U+FG}$ is the total energy of a lattice containing one fission gas substitutional atom, $E_{nU}$ is the total energy of an ideal uranium supercell containing n lattice sites, and $E_{FG}$ is the energy of one fission gas atom in the face-centered cubic phase.

The formation energy of an interstitial fission gas defect is defined as

$$E_I = E_{nU+FG} - E_{nU} - E_{FG} \quad (7)$$

where $E_{nU+FG}$ is the total energy of nU atoms and one fission gas interstitial atom. The incorporation energy of a fission gas atom is calculated according to Nerikar [28] as

$$E_{inc} = E_{nU+FG} - E_{(n+1)U} - E_{FG} \quad (8)$$

where $E_{nU+FG}$ is the total energy of the cell with the fission product at a particular defect site, $E_{(n+1)U}$ is the total energy of the cell with a uranium atom at a particular defect site, and $E_{FG}$ is the energy of a single fission gas atom in the reference state. The incorporation energy does not account for the formation of the defect site and assumes there is always an excess of available defect sites. A positive value of the incorporation energy means energy is required for a fission product to be placed at a particular defect site.

One issue that arises when calculating defects in U is due to the large cutoff radius of the pseudopotential used. When a defect is present and the atoms are relaxed, adjacent pseudopotential cores may overlap. A large enough core overlap can make the supercell unstable, yielding unrealistic results for the relaxed structure. Another source of anomalous structural lattice relaxation around defects is the inherent mechanical instability of the bcc allotrope of U at 0 K. In order to avoid these instabilities, geometric relaxations are not performed for the whole supercell, but for a cluster of atoms that

consists of several fully symmetric layers of nearest neighboring atoms around the defect of interest. Meanwhile, all atoms in the supercell participate in the electron density optimization. This computational strategy is illustrated in figure 5 for the interstitial in the <100> dumbbell configuration. The supercell consists of 129 atoms, all of which contribute into the electronic density optimization. The geometric optimization is performed for an inner shell of atoms with unconstrained positions that consists of two nearest neighboring layers surrounding the interstitial. The energy of the relaxed configuration $E_{(n+1)U}$ and the interstitial formation energy are connected by equation 2.

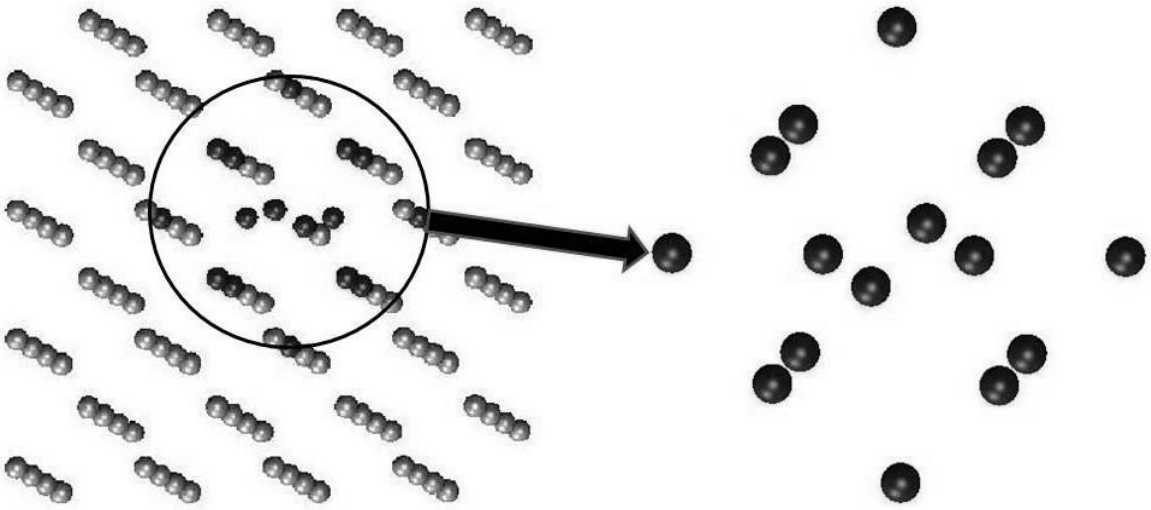

Figure 5. Schematic of the geometry used for calculating the formation energy of a <100> oriented dumbbell interstitial for a supercell with 129 atoms. Unconstrained atoms are shown as dark and constrained atoms as light. The relaxing inner shell consists of the two nearest neighbor full atomic layers surrounding the interstitial and is shown separately on the right.

This procedure is followed for all defect configurations in bcc U. The choice of the shell atomic configuration for each specific defect depends on the nature of the defect as well on its symmetry. Typically, two symmetric nearest neighboring atomic layers around the defects of interest (interstitial or vacancy) were taken and these atoms were considered unconstrained during the geometric optimization. Such a procedure produces uniform, symmetrical relaxation of the defect structure and prevents any spurious reorientation of the defect caused by pseudopotential core overlap and supercell instabilities.

## Molecular Statics and Dynamics Calculations

The Embedded-Atom Method (EAM) [38-40] has been shown to predict the properties of alloys and metals quite well. The EAM is the most widely used semi-empirical potential, with applications including calculations of point defects[41], melting [42], grain boundary structure and energy [43], dislocations [44], segregation [45], fracture [46] and surface structure [47]. The basis of the EAM is that the cohesive energy can be expressed in terms of embedding energies. In this view, each atom in the metal is embedded into the electron gas created by the other atoms. The EAM provides a robust means of calculating structure and energetics; however, it is best suited strictly for purely metallic systems with no directional bonding.

From the EAM, the total energy of a system of atoms is given by equation 9:

$$E = \sum_i \left\{ F(\overline{\rho}_i) + \frac{1}{2} \sum_{j \neq i} \varphi(R_{ij}) \right\} \quad (9)$$

where *i* and *j* are the individual atoms of the model [38, 39]. The pair interaction between atoms *i* and *j* is given by $\varphi$ [22]and is dependent on the separation between the atoms $R_{ij}$.

$$\varphi(R) = \frac{2}{Z}\left\{E^u(R) - F\left(\frac{\bar{\rho}^0(R)}{Z}\right)\right\} \tag{10}$$

In equation 10, $Z$ is the number of first neighbors, $\bar{\rho}^0(R)$ is the background electron density and $E^u(R)$ is the per atom energy of the reference structure as a function of nearest-neighbor distance $R$ [21] obtained from the universal equation of state of Rose et al. [47] given in equation 11.

$$E^u(R) = -E_c\left(1 + a^* + \delta \times \left(\frac{r_e}{r}\right) \times (a^*)^3\right) e^{(-a^*)} \tag{11}$$

with

$$a^* = \alpha\left(\frac{R}{r_e} - 1\right) \tag{12}$$

and

$$\alpha^2 = \frac{9\omega B}{E_c} \tag{13}$$

where $E_c$, $r_e$, $\omega$ and $B$ are the cohesive energy, nearest neighbor distance, atomic volume and bulk modulus, respectively, evaluated at equilibrium in the reference structure. In this work, the reference structure is taken as face-centered cubic, resulting in:

$$\bar{\rho}^0(R) = Z\rho^{a(0)}(R) \tag{14}$$

where $\rho^{a(0)}$ is an atomic electron density discussed below. The embedding function, *F*, is given in equation 15 and is the energy required to embed atom *i* into a system with a background electron density $\bar{\rho}_i$.

$$F(\bar{\rho}) = AE_c\frac{\bar{\rho}}{Z}\ln\frac{\bar{\rho}}{Z} \tag{15}$$

For this work, $Z = \rho_0 = 12$. The modification to the EAM is a function of how the electron density at a certain point, $\rho_i$, is calculated. In the traditional EAM, $\rho_i$ is simply the linear supposition of spherically averaged atomic electron densities:

$$\rho_i^{(0)} = \sum_{j\neq i}\rho_j^{a(0)}(R_{ij}) \tag{16}$$

whereas the MEAM introduces angularly dependent terms to augment $\bar{\rho}_i$ as shown in equations 17, 18 and 19 [22, 48].

$$(\rho_i^{(1)})^2 = \sum_\alpha \left\{ \sum_{j\neq i} x_{ij}^\alpha \rho_i^{a(1)} R_{ij} \right\}^2 = \sum_{j.k\neq i} \rho_j^{a(1)}(R_{ij}) \rho_k^{a(1)}(R_{ik}) \cos\{\theta_{ijk}\} \quad (17)$$

$$(\rho_i^{(2)})^2 = \sum_{\alpha,\beta} \left\{ \sum_{j\neq i} x_{ij}^\alpha x_{ij}^\beta \rho_j^{a(2)}(R_{ij}) \right\}^2 - \frac{1}{3} \sum_{j\neq i} \left[ \rho_j^{a(2)}(R_{ij}) \right]^2 \quad (18)$$

$$(\rho_i^{(3)})^2 = \sum_{\alpha,\beta,\gamma} \left\{ \sum_{j\neq i} x_{ij}^\alpha x_{ij}^\beta x_{ij}^\gamma \rho_j^{a(3)}(R_{ij}) \right\}^2 - \frac{3}{5} \sum_{j\neq i} \left[ \rho^{a(3)}(R_{ij}) \right]^2 \quad (19)$$

Here, the $\rho^{a(l)}$ are the atomic densities which represent the decrease in the contribution with distance $R_{ij}$ and the α, β, γ summations are each over the three coordinate directions with $x_{ij}^\alpha$ being the distance the ratio $R_{ij}^\alpha$/R$_{ij}$ with $R_{ij}^\alpha$ being the α component of the distance vector between atoms *i* and *j* [22]. Similar to equation 14, equations 15 and 16 can be put in a form that has a dependence on the angle between atoms *i*,*j* and *k* ($\theta_{ijk}$), and this has been done by Baskes et al. [49]. Atomic electron densities are assumed to decrease exponentially,

$$\rho_i^{a(l)}(R) = e^{\left[-\beta^{(l)}\left(\frac{R}{r_e}-1\right)\right]} \quad (20)$$

where $\beta^{(l)}$ are the decay lengths. To obtain the background electron density from the partial electron densities we make the assumption that the angular terms are a small correction to the EAM.

$$(\rho_i^{(0)})^2 = \sum_{l=0}^{3} t_i^{(l)} (\rho_i^{(l)})^2 \quad (21)$$

Many body screening is implemented through a screening function, $S_{ik}$, that quantifies screening between two atoms *i* and *k* due to other atoms in the system, *j*. The atomic electron densities and the pair potential are multiplied by this function. The screening function depends on all other atoms in the system:

$$S_{ik} = \prod_{j\neq i,k} S_{ijk} \quad (22)$$

where $S_{ijk}$ is calculated using a simple geometric construction. The screening factor $S_{ijk}$ is defined as:

$$S_{ijk} = f_c\left[\frac{C-C_{min}}{C_{max}-C_{min}}\right] \tag{23}$$

where C is a geometric parameter, and $C_{min}$ and $C_{max}$ are limiting values of C. The smooth cutoff function is:

$$f_c(x) = \begin{bmatrix} 1 & x \geq 1 \\ [1-(1-x)^6]^2 & 0 < x < 1 \\ 0 & x \leq 0 \end{bmatrix} \tag{24}$$

A radial cutoff function is also applied to the atomic electron densities and pair potential which is given by $f_c[(r_c - r)/\lambda]$ where $r_c$ is the cutoff distance of 4.5 Å and λ gives the cutoff region and was chosen to be 0.1. The MEAM has been shown to accurately predict the behavior of complex systems such as plutonium [21] and tin [50].

Using the above equations, a MEAM semi-empirical potential is developed for the high temperature body-centered cubic phase of uranium. The model parameters are fit to various physical properties of uranium metal obtained from experimental as well as first principles methods. The MEAM parameters and their respective sources are given in Table 1. The first column shows the parameter variables, while the second column gives the values. The third column shows the physical quantity that was used to optimize the value of the variable. Since the model parameters are highly correlated with a physical property, the parameters are varied one at a time to obtain the best fit to the experimental/first principles database (see Table 1). The fcc structure was chosen as the reference state. $E_c$, $r_e$, and α were initialized using the database and equation 9 for α. The parameter *A* was initialized at unity, the β's at six, the t's at zero, and delta at zero. The angular screening parameters were initialized at $C_{min}$=2 and $C_{max}$=2.8. Each parameter

was varied in turn to improve the agreement between the MEAM calculation and the relevant database property. For example, *A* was varied to establish agreement between the calculated energy difference between the relaxed α and γ phases and the database. All properties (except thermal expansion) were calculated for each change of parameters to ensure that the fit to the entire database did not deteriorate. Periodically during the fitting process δ was varied to match the experimental value of thermal expansion. Due to the weak correlation of the model parameters, this process converges rapidly. This fitting procedure was tailored specifically towards optimizing properties of the γ phase of U. Investigation of α U shows that this structure indeed possesses a lower cohesive energy per atom when compared to γ U, but shows large variance in internal coordinates and lattice parameters when compared to experiment.

Table 1. Parameters of the MEAM potential for γ U, the value of the parameters.

| **Parameter** | **Value** | **Source** |
|---|---|---|
| $E_c$ (eV) | 5.27 | Cohesive energy of α/γ*/fcc [27] |
| $r_e$ (Å) | 4.36 | Lattice constant of γ [51, 52] |
| α | 5.1 | Bulk modulus of γ [53] |
| A | 1.04 | Relative stability of α and γ [54] |
| $\beta^{(0)}$ | 6.0 | Relative stability of fcc and γ [54] |
| $\beta^{(1)}$ | 6.8 | Shear elastic constants of α [12] |
| $\beta^{(2)}$ | 7.0 | Shear elastic constants of α [12] and γ * |
| $\beta^{(3)}$ | 7.0 | Shear elastic constants of γ* |
| $t^{(1)}$ | 2.5 | Vacancy formation energy in γ [15] |
| $t^{(2)}$ | 4 | Shear elastic constants of α [12] and γ * |
| $t^{(3)}$ | 3 | Atomic volume of α [12] |
| δ | 0.1 | Thermal expansion of γ [52] |
| $C_{min}$ | 1 | Cohesive energy of α/γ*/fcc [27] |
| $C_{max}$ | 1.9 | Cohesive energy of α/γ*/fcc [27] |

*****Data from unpublished sources.

# CHAPTER 3

# BULK PROPERTIES AND INTRINSIC DEFECTS OF URANIUM

## Properties of defect free γ-U

First, properties of defect free γ-U are calculated and compared with those in literature. By varying the lattice constant and calculating the energy of the system, an energy–lattice parameter curve (Birch–Murnaghan curve) [55] is generated, allowing the calculation of the equilibrium bulk modulus. The Birch–Murnaghan curve is calculated for the PW91 GGA potential and the PBE GGA potential for various k-point meshes, starting with 1× 1 × 1 and increasing sequentially to 4×4×4, in a 128 atom supercell with periodic boundary conditions for γ -U. The minimum of this curve yields the equilibrium lattice parameter and the bulk modulus is calculated from

$$B = -\frac{\partial^2 E}{\partial V^2} V \qquad (25)$$

evaluated at the equilibrium lattice constant [56]. The bulk modulus was calculated with a Birch–Murnaghan curve fit for the entire total energy data (figure 6). Restricting the data set to a few points around the minimum produces changes in the bulk modulus of approximately 3%. The calculated Birch–Murnaghan curves for the PBE and PW91 functionals are shown in figures 6 and 7, respectively. Table 2 shows the lattice parameter, volume per atom, and bulk modulus calculated using both the PBE and PW91 functionals for different k-point meshes. Also shown for comparison are the values calculated by Xiang et al. [14] and Taylor [12] as well as the experimental values determined by Yoo et al. [7]. The values for the lattice parameter are within 1% of the literature values.

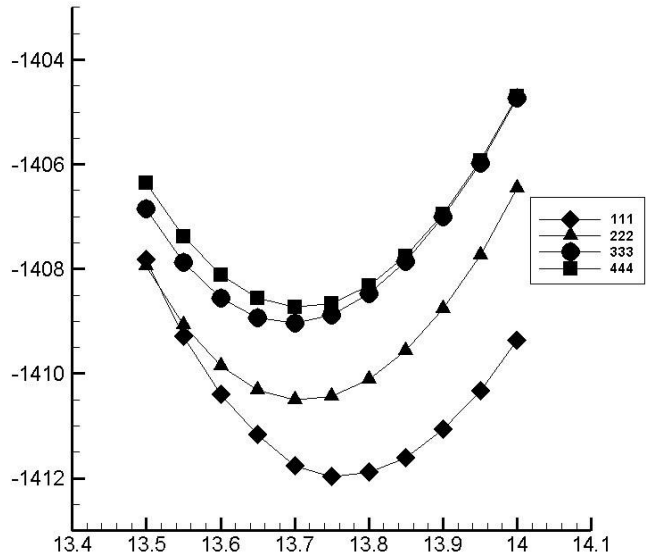


Figure 6. The total energy of the perfect bcc uranium lattice as a function of the supercell lattice parameter. Calculations were performed with the PBE exchange correlation functional for different k-point meshes (1x1x1, 2x2x2, 3x3x3 and 4x4x4).

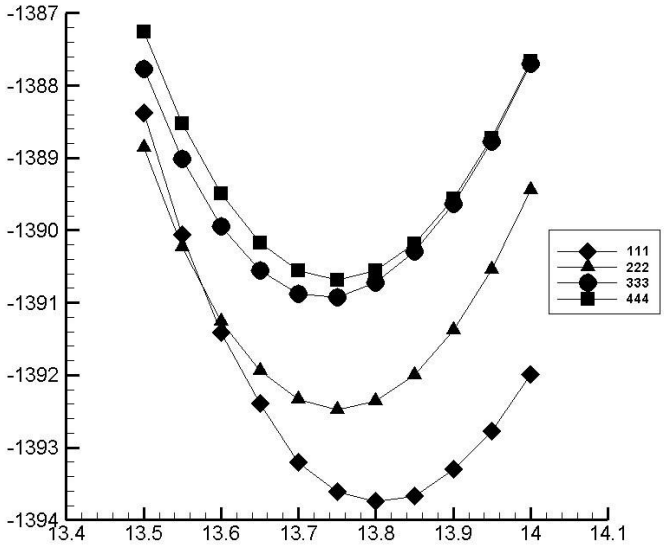


Figure 7. The total energy of the perfect bcc uranium lattice as a function of the supercell lattice parameter. Calculations were performed with the PW91 exchange correlation functional for different k-point meshes (1x1x1, 2x2x2, 3x3x3 and 4x4x4).

Table 2. The properties of defect free b.c.c U: the lattice constant, volume per atom and bulk modulus. Results for both the PBE and PW91 functionals and different k-point meshes (1x1x1, 2x2x2, 3x3x3 and 4x4x4) are shown. The results are compared with the work of Xiang [14], Taylor [12] and the experimental work of Yoo [7].

| | | $a_0$ (Å) | V (Å$^3$) | B (GPa) |
|---|---|---|---|---|
| 111 | PBE | 3.4418 | 20.39 | 138.29 |
| | PW91 | 3.4525 | 20.58 | 133.41 |
| 222 | PBE | 3.4275 | 20.13 | 133.07 |
| | PW91 | 3.4390 | 20.34 | 130.41 |
| 333 | PBE | 3.4235 | 20.06 | 136.29 |
| | PW91 | 3.4338 | 20.24 | 133.16 |
| 444 | PBE | 3.4283 | 20.15 | 133.64 |
| | PW91 | 3.4383 | 20.32 | 133.03 |
| Xiang | | 3.4313 | 20.20 | 122.6 |
| Taylor | | 3.43 | 20.18 | 176 |
| Expt | | 3.419 | 19.98 | 113.3 |

The bulk modulus values agree better with the calculations by Xiang [14] than those by Taylor [12] and slightly overestimate the experimental value of Yoo [7]. There is a significant difference between the calculated total energies for different exchange-correlation functionals, but the values of the equilibrium lattice constant and the bulk modulus are similar for the two pseudopotentials. Increasing the density of the k-point mesh for each pseudopotential increases the total energies of the lattice, but this effect is less pronounced for finer k-point meshes. There is a general trend for the coarser k-point mesh to yield a curve that has a slightly larger lattice constant than for finer mesh grids. Likewise, the PW91 functional gives a slightly higher equilibrium lattice constant for all of the tested k-points.

**Defect formation energies in γ-U**

Using the equilibrium lattice parameters calculated from the analysis of defect free U, a single atom is removed from the supercell and a structural optimization is performed, where fourteen atoms (two shells) are allowed to relax. In table 3, the calculated vacancy formation energy for the PBE and PW91 functionals are compared with the experiment [15] as well as with the computational results of Xiang et al. [14].

Table 3. The formation energy of vacancies in bcc U calculated using both the PBE and PW91 functionals and a k-point mesh of 4x4x4. The vacancy formation energies estimated from positron annihilation spectroscopy measurements [15] and calculated by Xiang [14] are also shown.

| | |
|---|---|
| $E^{v}_{form}$ (PBE) | 1.384 eV |
| $E^{v}_{form}$ (PW91) | 1.323 eV |
| $E^{v}_{form}$ (Xiang) [14] | 1.08 eV |
| $E^{v}_{form}$ (Matter) [15] | 1.2 ± 0.25 eV |

The vacancy formation energy is about 0.3 eV higher than that calculated by Xiang using a 54 atom simulation cell and PBE exchange-correlation functionals. However, results from this work are in good agreement (within the experimental error) with experiments of Matter et al. [15], who measured the positron annihilation coincidence count rate as a function of temperature and analyzed the data in terms of the trapping model, yielding relatively accurate values for the monovacancy formation energy.

For the calculation of interstitials, a single U atom is added into the supercell in different positions to calculate the formation energy from equation 3. In figure 8, the calculated interstitial formation energies for the PBE xc-functional are presented. Figure

8 also shows the atomic structure of the relaxed shell of atoms around the defect. First, it is interesting to compare the relative magnitudes of the interstitial formation energies. The formation energy of the dumbbell interstitial is heavily dependent on the orientation of the defect, with the <111> direction having a formation energy nearly three times higher than either of the other dumbbell orientations. The <100> dumbbell, <110> dumbbell, and octahedral have the lowest formation energies, all below 1 eV. Thus, these configurations are predicted to be the most prevalent self-interstitials. Also noteworthy is the order of magnitude of the formation energies for interstitials. Typical formation energies for similar interstitial defects in transition metals are of the order of several electron volts. The methodology of relaxing symmetric layered shells implemented here is not exact, and will typically overestimate the formation energy of defects, i.e., the real formation energy should be lower than presented results. However, the fact that the formation energy of interstitials is comparable to the formation energy of vacancies is significant, since it implies similar equilibrium concentrations for these different classes of defects. The difficulty of the extraction of interstitial formation energies from experiment restricts verification of these results to previous computational work, which consists of calculations of vacancy formation energies only [15]. Of actinide metals, point defect properties of Pu have been studied. Using modified embedded-atom methods to describe interatomic interactions in plutonium, Berlu et al. [57] and Valone et al. [58] have calculated low interstitial formation energies in α- Pu. All calculated Pu self-defect dumbbell configurations and the octahedral configuration had formation energies of below 1.7 eV.

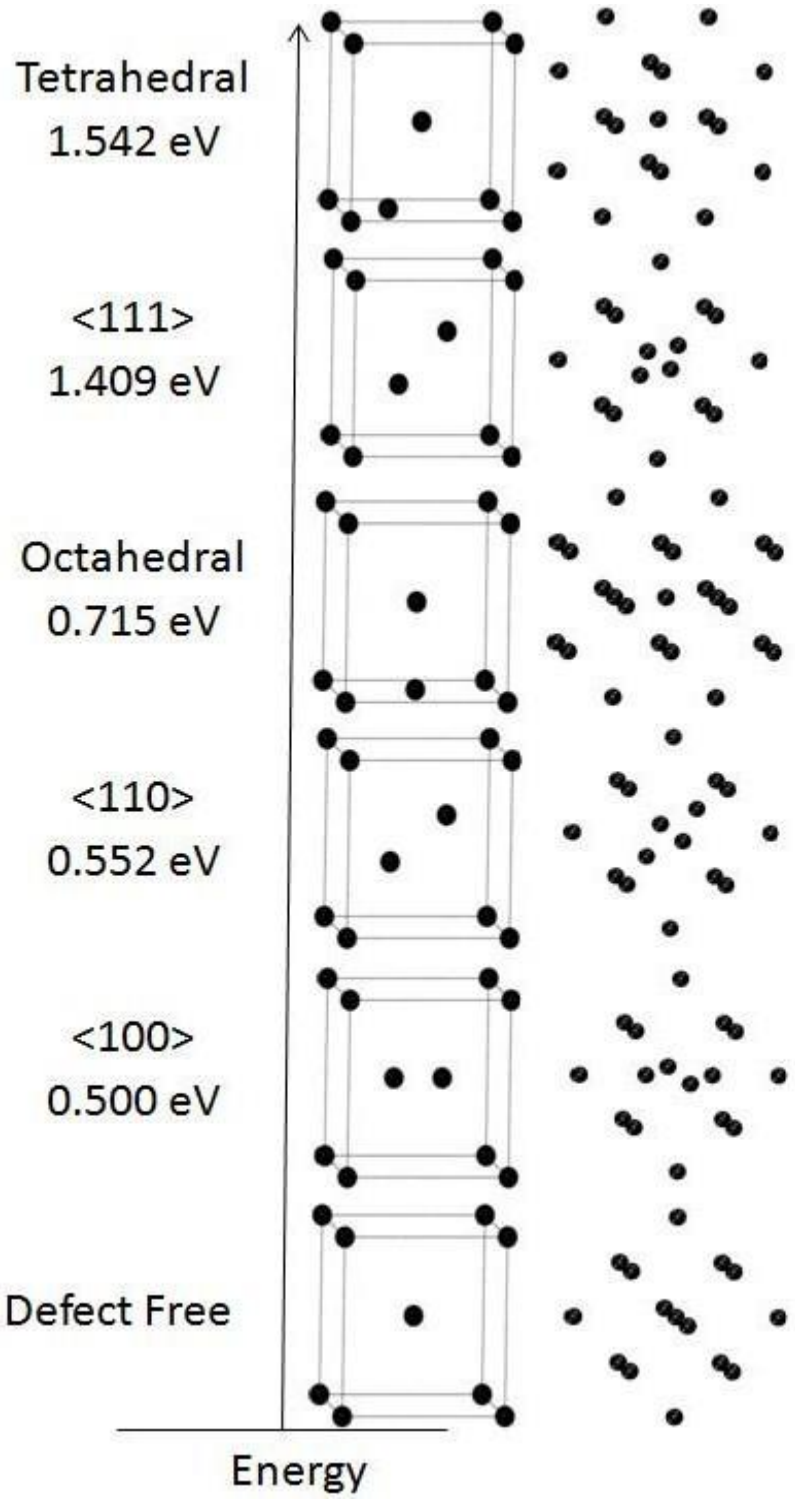


Figure 8. Self-defect formation energies calculated using the PBE exchange-correlation functional and a k-point mesh of 4x4x4. Also shown are corresponding relaxed atomic configurations for different uranium interstitials in the bcc γ-U allotrope.

**Defect formation energies in α-U**

The face-centered orthorhombic unit cell of α-U is shown in figure 9. The α phase has a face-centered orthorhombic structure, and its conventional unit cell contains four atoms, as in face-centered cubic (fcc) crystals. However, the atoms at some traditional face-centered sites are not face centers although they are on front and back faces. Further, there are no atoms on two faces of the cube; instead, one effective atom resides inside the unit cell.

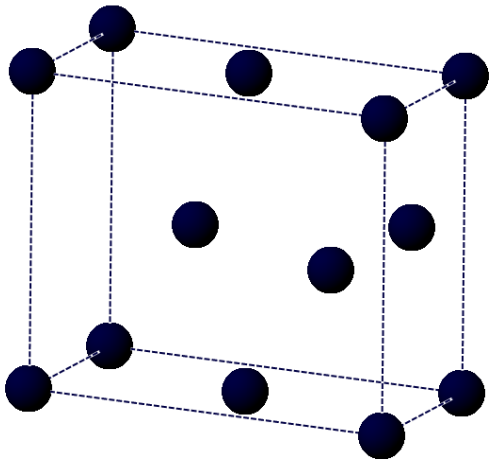

Figure 9. Schematic of the face-centered orthorhombic (A20) crystal structure of α-U.

For the analysis of α-U, a 4 × 2 × 3 supercell with 96 atoms is used. A relaxation is performed for the entire supercell, allowing the atoms themselves to relax, and also allowing the volume and shape of the supercell to change, starting with the equilibrium lattice parameters calculated by Taylor [12] and utilizing only the PBE description of the exchange-correlation functional. In table 4, the calculated equilibrium lattice parameters, volume per atom and the vacancy formation energy are compared with the results of Taylor [12]. The vacancy formation energy was also calculated to be 1.69 eV by Huang [16].

Table 4. The lattice parameters (a, b, c and y), volume per atom and the vacancy formation energy calculated for the orthorhombic α allotrope of uranium using the PBE functional and a k-point mesh of 4x4x4. The calculated vacancy formation is compared with the results of Taylor [12].

| | Taylor [12] | This Work |
|---|---|---|
| a (Å) | 2.800 | 2.793 |
| b (Å) | 5.896 | 5.845 |
| c (Å) | 4.893 | 4.896 |
| y | 0.097 | 0.099 |
| Volume/atom ($Å^3$) | 20.19 | 19.98 |
| $E^v_{form}$ (eV) | 1.95 | 1.86 |

Four interstitial structures were analyzed in the α phase of uranium: free space, and the <100>, <010> and <001> split dumbbell interstitials. The crystal structure of α-U has a relatively large open volume, placing an interstitial in this open volume is referred to as the free space defect, shown in figure 10. Split dumbbell interstitials for all three orientations are shown in figure 11.

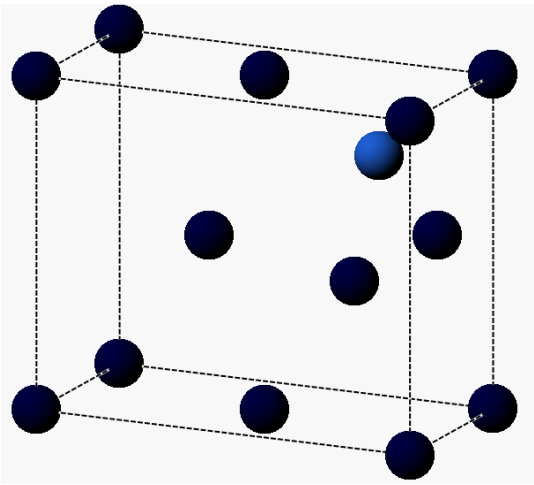

Figure 10. The free space defect in α-U. The α phase of U has a large open volume, placing a defect in the center of this open volume denotes a free space defect. Internal

coordinates of the free space defect are (0.5, 0.812, 0.8) where the unit cell dimensions are (2.8, 5.896, 4.893). The free space defect is illustrated as the light blue atom.

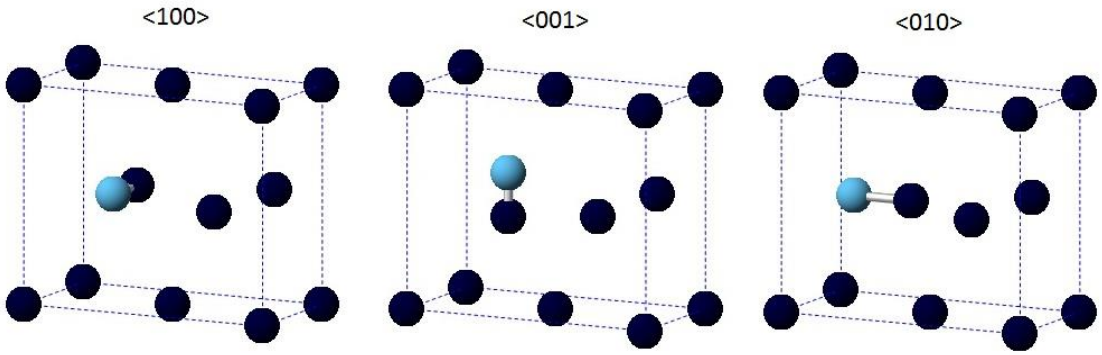


Figure 11. Schematic of split dumbbell interstitials in α-U. Three orientations of split dumbbell interstitials were analyzed: <100>, <010>, and <001>. Due to the anisotropy of the A20 structure, these three dumbbells represent very different defect configurations.

In table 5, the calculated self-interstitial formation energies in α-U are presented. The formation energies in α-U are greater than in γ-U due to α-U being a more closely-packed structure. The open volumes to incorporate defects in γ-U are larger than those in α-U. Thus, it is expected to be more difficult to create a defect in α-U, leading to higher formation energies of intrinsic and extrinsic defects. These values are slightly underestimated when compared to Huang [16], who calculated the formation energy of the free space defect to be 4.42 eV.

Table 5. Formation energy (eV) of self-interstitials in orthorhombic α uranium for the defect configurations corresponding to those in figures 6 and 7.

| | $E_f$ |
|---|---|
| Free space | 3.53 |
| <010> | 3.87 |
| <001> | 3.62 |

# CHAPTER 4

# PROPERTIES OF EXTRINSIC DEFECTS IN URANIUM

## Dilute Zr defect formation energies in γ-U

Using the equilibrium lattice parameters calculated from the analysis of defect free γ-U, a single Zr atom was added into the supercell as part of a defect configuration and a structural optimization was performed. In figure 12, the calculated Zr defect formation energies for the PBE functional are presented. It is important to note that the formation energy of a substitutional defect is much lower than any configuration with an interstitial Zr atom. Thus, the substitutional position is the preferred location of dilute Zr atoms in γ-U. During irradiation, Zr may be knocked off its lattice site and occupy interstitial locations in the U–Zr lattice. These calculations show the <110> dumbbell as the lowest energy configuration for such a knocked off Zr interstitial. The tetrahedral and the <111> dumbbells are the least favorable as they have the highest formation energy.

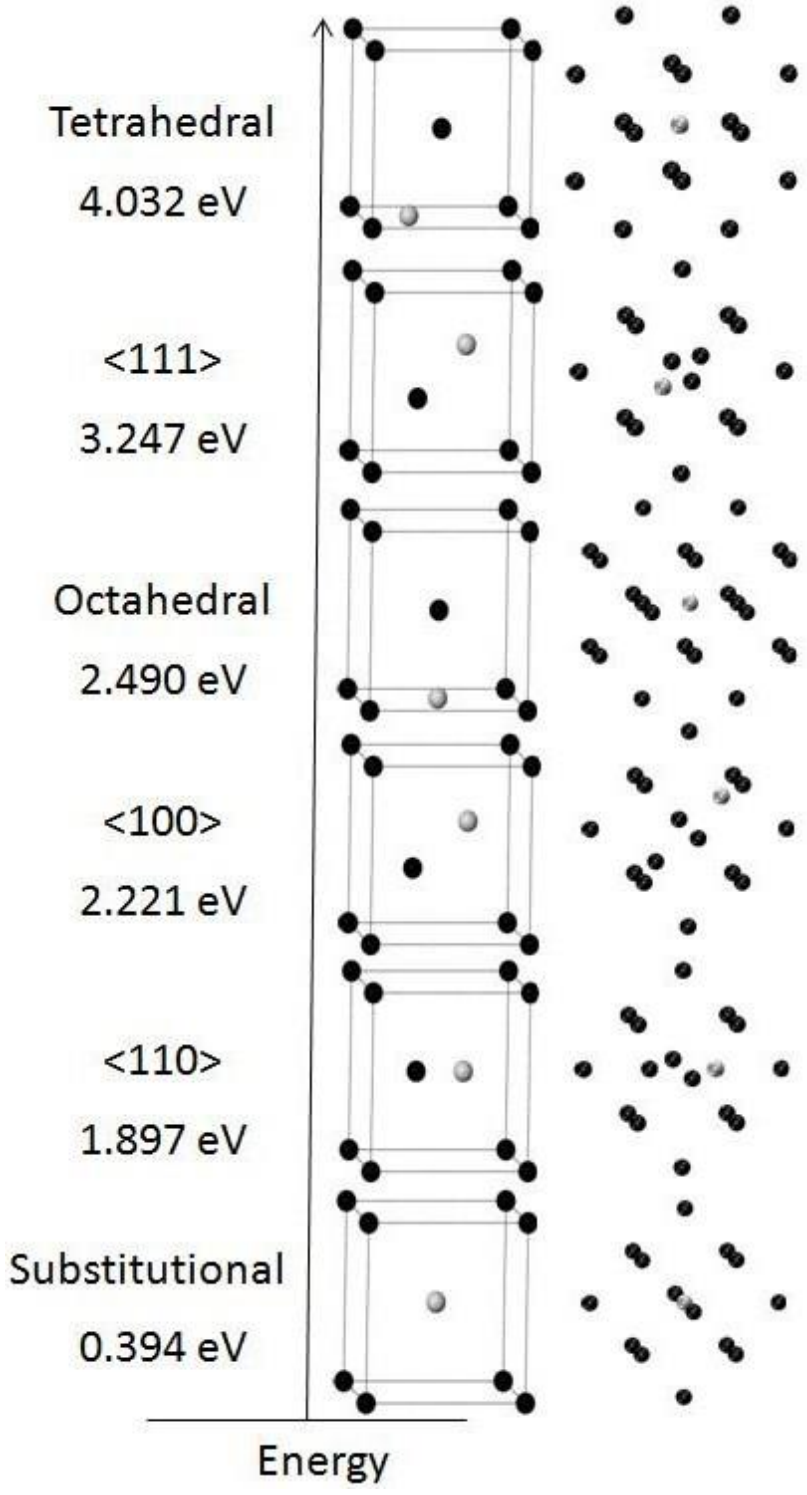


Figure 12. Zr defect formation energies calculated using the PBE functional and a k-point mesh of 4x4x4. Also shown are corresponding atomic figurations for possible Zr (white atoms) in the bcc γ-U phase.

**Fission Gas Defect Formation Energies and Incorporation Energies in γ-U**

Using the equilibrium lattice parameters calculated from the analysis of defect free bcc U, a single fission gas atom is added into the supercell to calculate the formation energy using equations 6 and 7. In table 6, the calculated substitutional and interstitial formation energies are presented and plotted graphically in figure 13.

Table 6. Formation energies (eV) of He, Xe and Kr in body-centered cubic uranium for the substitutional, <100>, <110> <111> dumbbells and the octahedral and tetrahedral interstitial positions.

| | He | Xe | Kr |
|---|---|---|---|
| Sub | 1.803 | 5.549 | 5.926 |
| <100> | 2.234 | 7.294 | 6.549 |
| <110> | 2.148 | 7.037 | 7.345 |
| <111> | 1.764 | 10.085 | 8.420 |
| Octahedral | 2.507 | 7.024 | 6.210 |
| Tetrahedral | 2.434 | 7.730 | 7.002 |

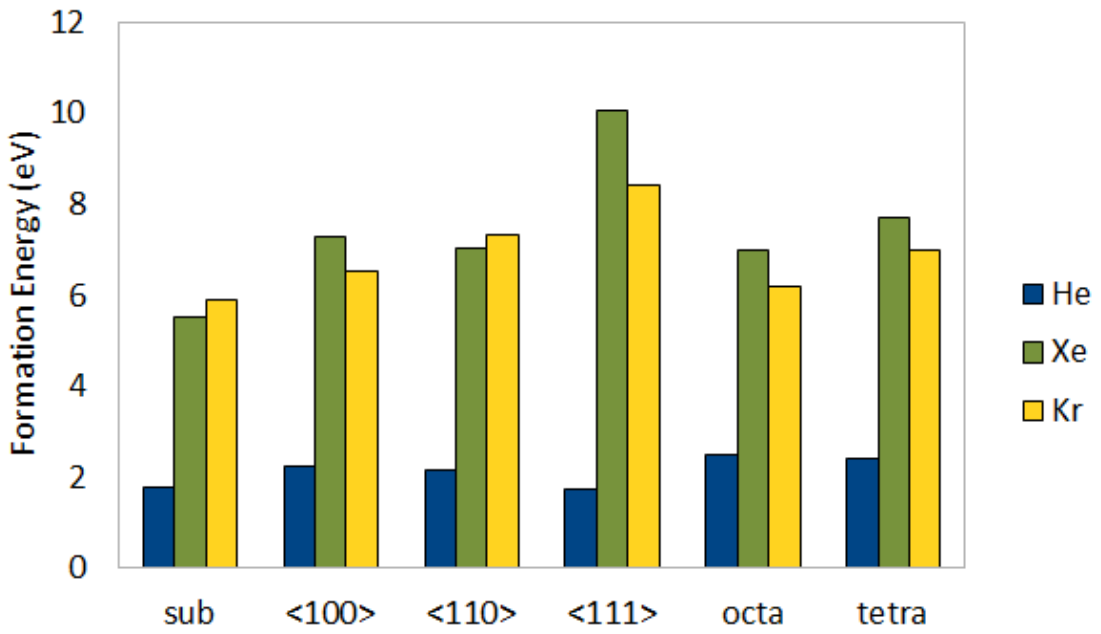


Figure 13. Formation energies (eV) of He, Xe and Kr in body-centered cubic uranium. The six positions considered are the same as the six position shown in figure 4, namely substitutional, octahedral, tetrahedral and the <100>, <110> and the <111> dumbbells.

The incorporation energies are calculated from equation 8 using uranium self-defect calculations in figure 4. In table 7, the calculated fission gas defect incorporation energies are presented and shown graphically in figure 14.

Table 7. Incorporation energies (eV) of He, Xe and Kr in body-centered cubic uranium for the same configurations as in table 6. Self-defect energies are obtained from table 5 and equation 8 is used to calculate the incorporation energies.

| | He | Xe | Kr |
|---|---|---|---|
| Sub | 1.803 | 5.549 | 5.926 |
| <100> | 11.312 | 17.752 | 17.007 |
| <110> | 11.279 | 17.548 | 17.855 |
| <111> | 9.986 | 19.686 | 18.020 |
| Octahedral | 11.410 | 17.307 | 16.492 |
| Tetrahedral | 10.576 | 17.251 | 16.523 |

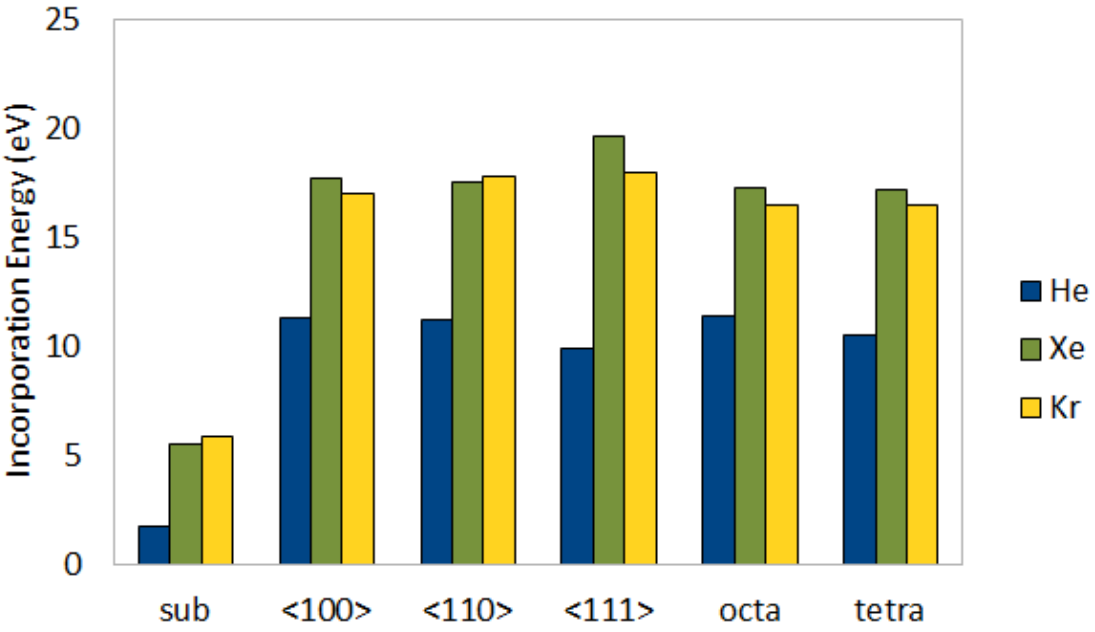


Figure 14. Incorporation energies (eV) of He, Xe and Kr in body-centered cubic uranium for the same configurations as in figure 9.

First, it is interesting to compare the relative magnitudes of the defect formation energies for each fission gas atom. There exists a general size effect with regards to the magnitude of formation energies of fission gas atoms. This is most pronounced when comparing helium with the other two species. Helium is a relatively small atom (atomic radius: 31pm[59]) and thus it is expected that the defect formation energies for He are much lower than those of Xe and Kr, which are larger atoms (atomic radius: 108pm and 88pm, respectively[59]). Also, helium formation energies in the substitutional and interstitial positions do not vary much in magnitude. In the case of the much larger Xe and Kr, it is clear that these fission products prefer to reside in the vacant lattice site rather than in an interstitial position.

This size effect is also seen in most cases while comparing Xe and Kr (Xe having the greater size), except in the case of the substitutional defect and the <110> dumbbell interstitial. This is possibly due to the very small difference between the two pseudopotential core radii, which is less than 0.11 Å (Xe core radius is 1.323 Å and Kr core radius is 1.217 Å). Also, the shell methodology is an approximation technique and there are inherent errors associated with using this technique for an energy minimization.

Valuable information can be also gleaned by analyzing the relative magnitudes of the different defect configurations. There is a total variance of approximately 0.75 eV from the most energetically favorable defect configuration to the most energetically unfavorable configuration for He. Thus, it is expected that He will be found in a variety of defect positions in bcc U. For Xe and Kr, the formation energy of the defect is heavily dependent on the orientation, with the <111> dumbbell having the highest formation energy and the substitutional site the lowest for both elements. Thus, the <111>

dumbbell configuration is predicted to be the least prevalent defect type and the substitutional the most prevalent. It makes physical sense that a substitutional defect would have the lowest formation energy, as a vacant uranium lattice position has a much greater volume than any other defect site. Thus, the overall localized deformation will be minimized by Xe or Kr inhabiting a vacancy. The formation energy of all fission gas defects in γ-U is larger than self-defects. The maximum self-defect formation energy has been calculated to be approximately 1.5 eV (figure 4), whereas the minimum He defect formation energy is 1.76 eV. Thus, it is more energetically favorable for bcc U to form a self-defect, than to form a fission gas defect. The shell methodology employed will typically overestimate the formation energy of defects, i.e., the formation energy should be lower than the values presented here.

The octahedral-tetrahedral migration mechanism seems appropriate for fission gases based on the energies of these respective defect configurations. Energy differences between these two configurations are below 0.8 eV for all fission product species. Given that an octahedral or tetrahedral defect is present, fission product diffusion is likely to occur via this mechanism. The difficulty of the extraction of interstitial formation energies from experiment and the lack of previous computational work on fission gas defects in metallic uranium means there is no comparison for benchmarking these values. On the basis of these results, it is expected that Xe and Kr would occupy vacant U lattice sites rather than interstitial positions. Also, it is apparent that helium may be found in either substitutional or interstitial positions with the difference in energies of these configurations being much smaller. While no calculations of the migration energy were performed, it is apparent that helium would be a more mobile species, with transitions

from interstitial to substitutional and vice versa resulting in less energy differences. It would be expected that Xe and Kr would migrate by a substitutional vacancy exchange mechanism, with relatively high values of the migration barrier for such an exchange. Given the computational complexity, it is not yet possible to perform calculations of the migration pathway using DFT methods.

**Fission Gas Defect Formation Energies and Incorporation Energies in α-U**

In table 8, the calculated substitutional and interstitial formation energies for defects in α-U are presented and shown in figure 15. In order to calculate incorporation energies of fission gas defects in α-U, self-defect formation energies of defects in α-U are needed. Self-defect formation energies are given in table 5.

Table 8. Formation energies (eV) of He, Xe and Kr in orthorhombic uranium for the substitutional, free space defect and the <010> and <001> dumbbell configurations.

| | He | Xe | Kr |
|---|---|---|---|
| Sub | 3.33 | 6.13 | 6.03 |
| Free space | 3.63 | 12.25 | 10.26 |
| <010> | 3.82 | 11.58 | 10.17 |
| <001> | 3.65 | 10.65 | 9.63 |

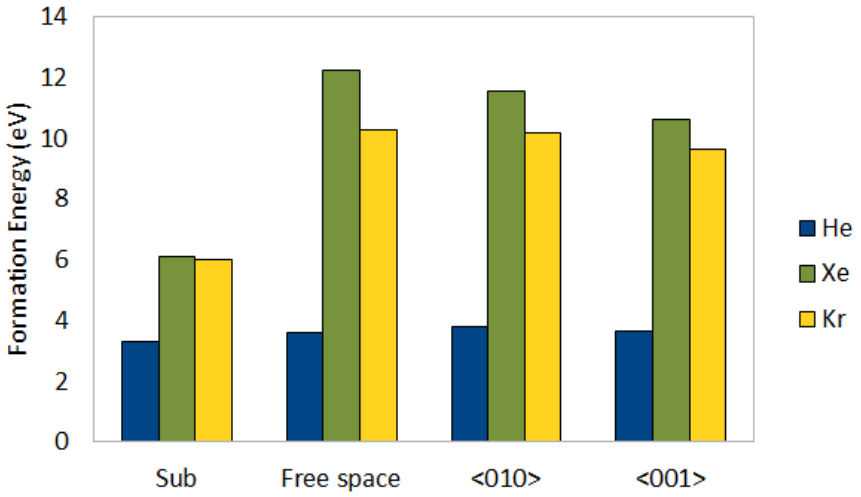


Figure 15. Formation energies (eV) of He, Xe and Kr in orthorhombic uranium in the substitutional, free space defect and <100>, <010> and <001> configurations. These correspond to the configurations shown in figures 6 and 7 (substitutional is not shown).

Using the self-defect energies from table 5, the incorporation energies were computed and are presented in table 9 and figure 16.

Table 9. Incorporation energies (eV) of He, Xe and Kr in orthorhombic uranium obtained from equation 8 using data in tables 8 and 5.

| | He | Xe | Kr |
|---|---|---|---|
| Sub | 3.33 | 6.13 | 6.03 |
| Free space | 9.62 | 20.00 | 18.00 |
| <010> | 9.47 | 18.98 | 17.57 |
| <001> | 9.55 | 18.31 | 17.29 |

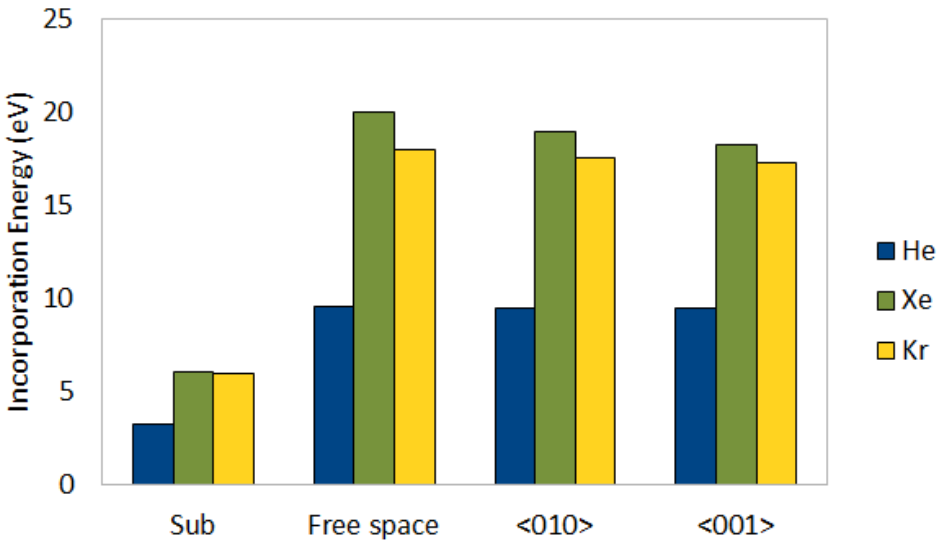


Figure 16. Incorporation energies (eV) of He, Xe and Kr in orthorhombic uranium for the configuration as described in figures 6, 7, and 11.

In α-U, similar trends are observed to those in γ-U for extrinsic gas defects. Helium exhibits the lowest formation energy of fission product species analyzed, with a variance of less than 0.5 eV between defect positions. Size effects appear to dominate formation energies for the α phase. Xenon is the largest fission product species analyzed and has the highest formation energies, while He is the smallest species investigated and has the lowest formation energies. For Xe and Kr, the substitutional site is the preferred defect location. It is interesting to note that formation energies of fission products in α-U are generally higher than those in γ-U. This results from α-U having a more closely-packed crystal structure than the γ phase. The octahedral and tetrahedral volumes in γ-U are larger than the free space defect volume in α-U. Also, α-U is a more rigid structure in terms of elastic constants, so it is expected that the formation of dumbbell interstitials would be more difficult than in γ-U. In comparing the formation energies of fission gases

to the self-defects, the Xe and Kr defects are less energetically favorable, but He formation energies are comparable.

The fuel undergoes phase transformations during initial operation as well as when it is cooled down. In addition, during operation, temperatures at the fuel pin periphery suggest that the alpha phase is present. Thus, the fact that formation energies of gas atoms are higher in the alpha U structure implies that the phase transformation from gamma to alpha may affect the fission gas behavior in the fuel. Higher formation energies imply higher strain fields associated with the defect incorporation leading to stress concentrators and incipient crack nucleation sites during reactor cool down and also during operation.

Comparisons can be made to a previous computational study of fission products in $UO_2$ [60]. A DFT based analysis of Xe in $UO_2$ yielded an incorporation energy of 11.11 eV for Xe interstitials. The work presented here has found that Xe interstitial incorporation energies in pure metallic U range from 17-20 eV, significantly higher than that for $UO_2$. The fluorite structure of $UO_2$ has a large open volume and thus can more readily include fission product defects. Thus, higher incorporation energies for pure metallic U are expected.

# CHAPTER 4

# MEAM INTERATOMIC POTENTIAL FOR γ URANIUM

## Molecular Statics Simulations

Using the interatomic potential developed above in chapter 2, calculations are performed for both the static ground state properties as well as high temperature properties of γ U. In the ground state, structural and elastic properties are calculated. The stability of the γ phase as a function of pressure is determined as well as the formation energy of a vacancy as a function of pressure. The calculations show that increasing pressure increases the stability of the γ phase. Increasing temperature increases entropy and also makes the γ phase stable. Molecular dynamics calculations of the γ phase at high temperatures are performed. Properties calculated include the melting point, enthalpy of fusion, heat capacity, thermal expansion and the volume change on melting. Vacancy and interstitial formation energies as a function of temperature are calculated to within 100 K of the melting point. The interatomic potential is shown to reproduce most properties satisfactorily. Details of calculations/simulations are presented below.

### Equilibrium lattice constant

Calculations were performed on systems of 2000 atoms for the γ (bcc) phase. Equilibrium lattice constants were calculated at 0 K by relaxing a defect free system with dynamic boundary conditions and a convergence criterion of less than $10^{-6}$ Å motion of any atom in an energy minimization iteration. In Table 10, the results are presented and compared to previous work using pseudopotentials as well as experimental values. The volume per atom and lattice constant are slightly overestimated in relation to previous

computational and experimental results. The experimental value is from Wilson [51] at a temperature of 1073 K. It is extrapolated to 0 K from a thermal expansion fit as shown by Basak [52].

Table 10. The equilibrium lattice constant at 0 K and the volume per atom at 0 K. Values are compared with the pseudopotential studies of Taylor[12], Crocombette et al. [11] and results presented above, full-potential (FP) calculations from Söderlind [9], as well as with an experimental value extrapolated to 0 K [51, 52].

| | MEAM | Taylor | Beeler | FP | Crocombette | Experiment |
|---|---|---|---|---|---|---|
| Method of estimation | Interatomic Potential | PAW Pseudopotential | PAW Pseudopotential | Linear Muffin Tin Orbital | Norm-conserving Pseudopotential | X-ray Diffraction |
| Lattice constant (Å) | 3.503 | 3.430 | 3.428 | 3.46 | 3.37 | 3.418 |
| Volume/Atom ($Å^3$) | 21.488 | 20.074 | 19.982 | 20.71 | 19.14 | 19.966 |

**Elastic constants**

Elastic constants were calculated at 0 K via analysis of the changes in internal energy due to small strains enforced on the lattice. The internal energy of a crystal system under strain was expanded in a Taylor series in powers of the strain tensor with respect to the initial energy of the unstrained crystal. Each elastic constant was computed from the application of a unique strain on the crystal, and the resulting change in internal energy. This methodology is outlined fully by Söderlind [9]. In this manner, the elastic constants $C_{11}$, $C_{12}$ and $C_{44}$ are obtained. The bulk modulus is calculated based on an elastic constant relationship for the body-centered cubic system ($B= (C_{11}+2C_{12})/3$). In Table 11, the elastic constants are presented and compared with previous computational studies utilizing pseudopotentials and full potential calculations, as well as a singular

experimental value. The bulk modulus compares very well to the experimental value. It is seen that the shear constant is less than zero at the ground state. This result implies mechanical instability at the ground state. This agrees with first principles calculations of Taylor [12], Eriksson [61] and Söderlind [54], all of whom predicted such instability. However, our value of C' (-3 GPa) is significantly less negative than that of Eriksson [61] (-60 GPa) but closer to Taylor [5] (-11 GPa).

Table 11. Elastic constants for γ uranium at 0 K. Values are compared with that of a pseudopotential study by Taylor[12], Full-Potential calculations by Eriksson[61] and experimental work by Yoo, et. al [53]. Units are in GPa.

| | MEAM | Taylor | Eriksson | Experiment |
|---|---|---|---|---|
| $C_{11}$ | 111 | 161 | - | - |
| $C_{12}$ | 117 | 184 | - | - |
| C' | -3 | -11 | -60 | - |
| $C_{44}$ | 15 | 56 | - | - |
| B | 115 | 176 | 125 | 113 |

**Elastic constants under hydrostatic pressure**

The application of pressure can stabilize γ uranium at low temperatures. The stability is analyzed through the elastic shear constant ($C' = (C_{11}-C_{12})/2$): if $C' < 0$, the system is unstable. In this methodology, the volume of a pure system is decreased incrementally, analogous to incrementally increasing pressure. At each pressure increment, the elastic constants are determined, allowing for the calculation of the shear constant. The elastic shear constant versus pressure at 0 K is displayed in Figure 17. The elastic shear constant becomes positive at 17.2 GPa, indicating the minimum pressure required to stabilize bcc U at 0 K. The stabilization of the γ phase with increasing pressure can be described as a function of the f-electron states. This behavior agrees well

with Eriksson's explanation of actinide metals [61, 62]. The crystal structures of actinides can be understood as a Peierls distortion, from the narrow f states situated close to the Fermi level. If the volume is reduced, the bandwidth is increased, and this effect becomes less important whereas the Madelung contribution to the energy will become increasingly important. This latter term stabilizes close-packed symmetric structures [62]. Also, Soderlind and co-workers [7, 10] investigated the generalized gradient approximation in combination with a full potential linear muffin-tin orbital technique to obtain the total energy differences for the b.c.t., fcc, bcc and hcp (ideal *c* /*a*) structures relative to the α U structure as functions of volume for U. At larger volumes, close to the equilibrium volume, they predict α U to be stable with the b.c.t. phase being very close in energy. However, when the metal is compressed, the bcc structure becomes stable over the hcp structure and finally over the α and b.c.t. structures as well. We show qualitatively similar results with the γ phase of uranium being stable at high pressures.

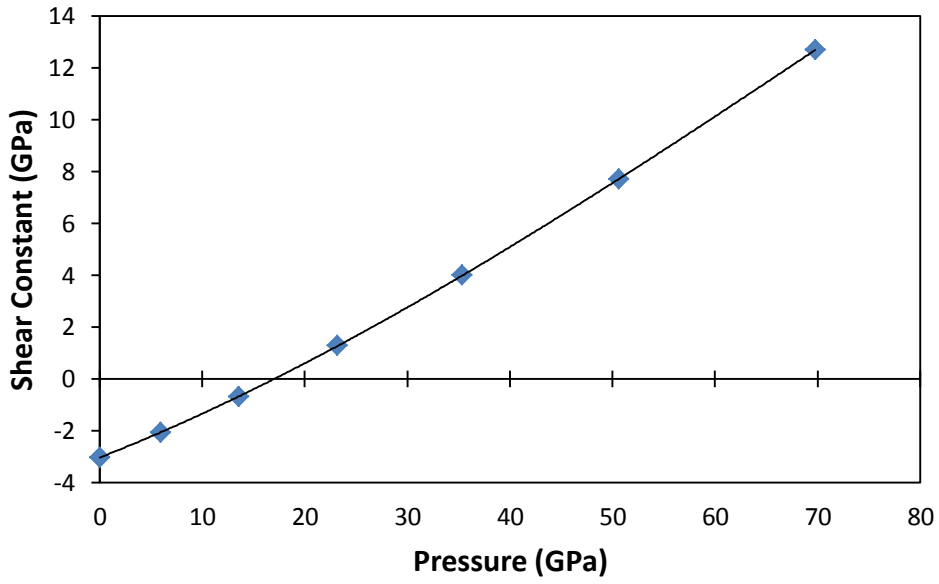


Figure 17. Shear constant of γ U as a function of hydrostatic pressure at 0 K. The shear constant is positive at a pressure higher than 17.2 GPa indicating a stable structure at 0 K.

**Vacancy formation energy as a function of pressure**

Introduction of a defect in the ground state at 0 K exacerbates the mechanical instability of γ U, creating changes in crystal structure and negative formation energies. Analysis of the vacancy formation energy versus pressure can serve to illustrate behavior and stability of γ uranium as well as providing relevant data regarding defect energetics. The vacancy formation energy was calculated from equation 2. The vacancy formation energy versus pressure is shown in Figure 18 for pressures where γ uranium is stable. The vacancy formation energy shows a linear trend versus pressure. Extrapolating to zero pressure generates an estimate for the equilibrium vacancy formation energy at 0 K. The extrapolation produces a vacancy formation energy of 1.61 eV. This compares very well to previous computational results presented above and experimental results from Matter [15] (1.2±0.25 eV).

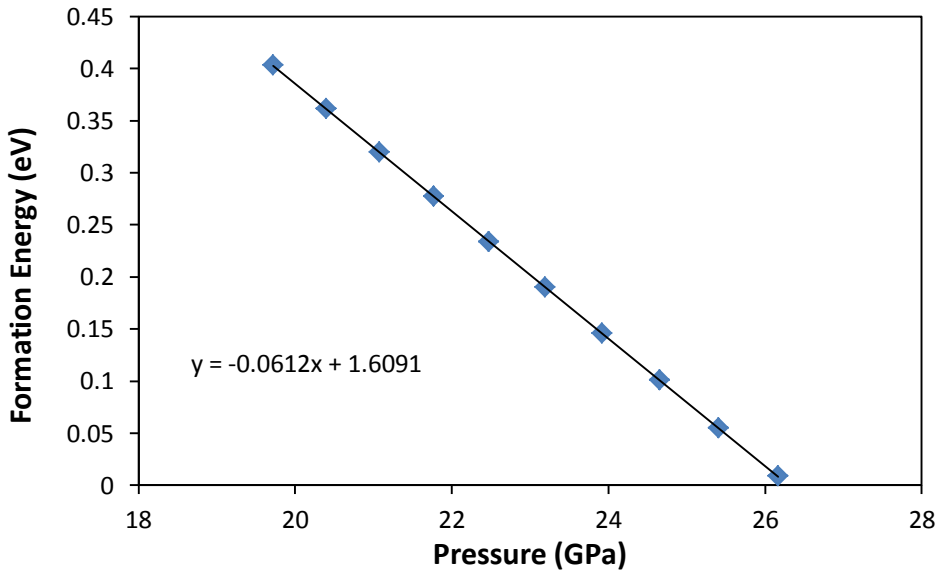


Figure 18. Vacancy formation energy versus hydrostatic pressure (eV vs. GPa). Calculations are performed for pressures greater than 17.2 GPa where the shear constant is positive indicating a stable γ phase.

## Molecular Dynamics Simulations

While above calculations illustrate that pressure stabilizes γ U at 0 K, the γ phase is the stable, highest temperature solid modification of uranium, as it is for a majority of the simple metals [63]. Bcc metals tend to have lower phonon energies and, thus, higher vibrational entropy than their fcc counterparts. Thus, γ U is the stable phase in equilibrium with the liquid. Calculations are performed on γ U at temperatures where the bcc structure is stable at ambient pressures, i.e., at 800 K and higher.

Molecular dynamics calculations are performed with a standard velocity Verlet integrator with a time step of 2 fs. The temperature was fixed using a Hoover drag with an approximate equilibration time of 0.1 ps. The energy, temperature and pressure of the system were output every 0.1 ps.

### Cohesive energy as a function of temperature

Dynamics calculations were performed on systems of 2000 atoms for the γ (bcc) phase. Equilibrium lattice constants were calculated by relaxing a defect free system with dynamic boundary conditions in an NPT ensemble for 50 ps, averaging over the final 20 ps of the simulation. Simulations were performed in increments of 100 K, from 100 K to 1500 K. The γ phase of U is stable from 800 K to the melting point. The cohesive energy as a function of temperature is shown in Figure 19. The cohesive energy was determined experimentally in the melting phase [27]. Cohesive energies in the solid phase were calculated using the experimental enthalpy of fusion and heat capacity [64]. In the body-centered cubic region, the cohesive energy is within 0.1 eV/atom of experiment, and displays approximately the same slope versus temperature as

experiment. For the liquid structure, the cohesive energy remains within 0.25 eV/atom of the experiment up to 2000 K.

**Melting temperature**

The melting temperature was calculated via an NPT ensemble with a solid/liquid interface and analyzing the evolution of the interface. Initially, a 20x5x5 supercell of γ U was equilibrated at 1200 K in an NPT ensemble to generate a crystal system at high temperature. Half the supercell was held at 1200 K and half was equilibrated at 2000 K in an NPT ensemble, restricting supercell shape change to the x-direction. This creates an interface of a crystal system and a liquid system. This interfacial structure can be equilibrated at various temperatures and through the analysis of the propagation of the interface, the melting temperature can be calculated. The interfacial structure is shown in Figure 20a. This structure is equilibrated for 1 ns at 1400 K to create Figure 20b, where the crystal structure has propagated throughout the entire supercell. The interfacial structure is equilibrated for 1ns at 1420 K to produce the system in Figure 20c, where the liquid structure has propagated throughout the entire supercell. The calculated melting temperature is 1410 K. The melting temperature is overestimated by only 2 K.

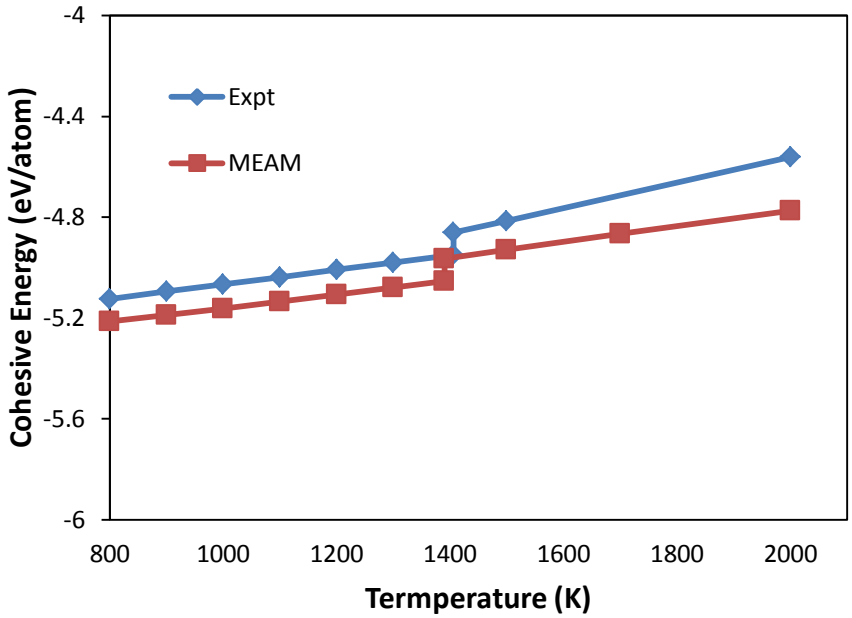


Figure 19. Cohesive energy of γ and liquid uranium in the temperature range 800-2000 K. The cohesive energy per atom is calculated in a 2000 atom supercell. Experimental curves are obtained from experimental enthalpy of fusion and heat capacity[64].

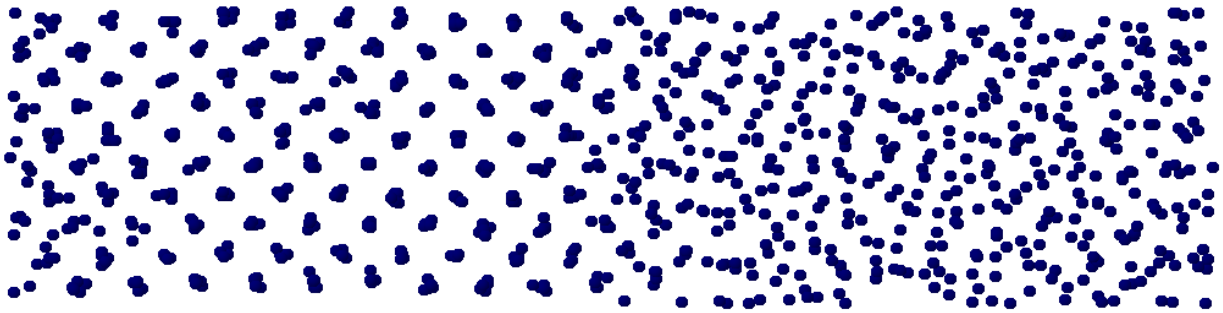

a) Half body-centered cubic, half liquid structure.

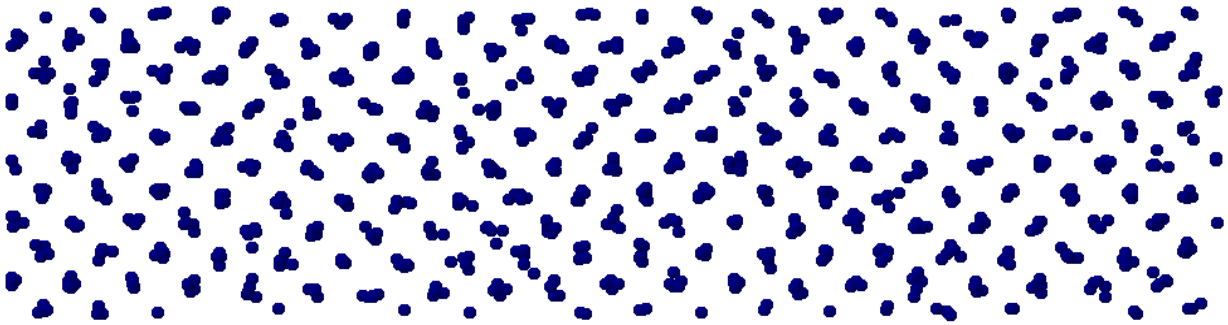

b) System (a) equilibrated for 1ns at 1400 K.

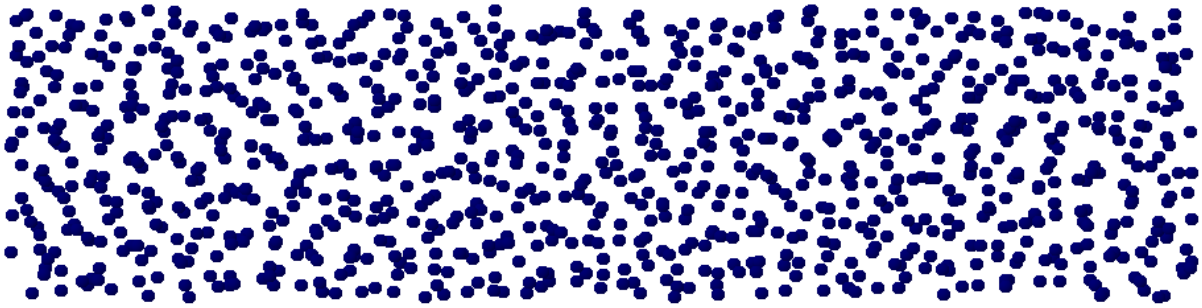

c) System (a) equilibrated for 1ns at 1420 K.

Figure 20. The γ-liquid interface, the γ phase at 1400 K and the liquid structure at 1420 K. Figure 20a is a half crystal-half liquid structure. Melting point is determined after equilibrating this system at the given temperature and analyzing the evolution of the crystal/liquid interface. Figure 20b was equilibrated at 1400 K (below melting point). Figure 20c was equilibrated at 1420 K (above melting point).

**Enthalpy of fusion**

The enthalpy of fusion was calculated as the energy difference between the crystalline and liquid systems. Initially, a defect free system was equilibrated in an NPT ensemble at 2000 K, well above the melting point, effectively melting the lattice. This liquid system was then equilibrated at 1410 K for 50ps, with energy and volume averages over the final 20ps. The results from these simulations were compared with crystalline γ U equilibrated at 1410 K for 50ps, with energy and volume averages over the final 20ps. The change in energy between the liquid system and the crystalline system, both equilibrated at 1410 K, is taken as the enthalpy of fusion. For the liquid and crystalline systems, eight simulations were performed to obtain statistical accuracy. The enthalpy of fusion for γ U is 8.66 ± 0.08 kJ/mol. This is in excellent agreement with the experimental

value of 8.5 kJ/mol. These same simulations are used to determine the volume change on melting. The volume change on melting is 2.17±0.78%. A literature review found there is no experimental value of the volume change on melting for comparison.

**Heat capacity at constant pressure**

In order to calculate the heat capacity, an NPT ensemble with 2000 atoms in the γ phase is equilibrated. The heat capacity is calculated as the change in total energy (potential + kinetic) divided by the change in temperature. The heat capacity varies slightly over the temperature range of stability, from 0.102 J/g-K (at 800 K) to 0.118 J/g-K (at 1400 K) increasing with increasing temperature. This range of values compares very favorably to the experimental value of 0.12 J/g-K [64].

**Thermal expansion**

The equilibrium volume was calculated as a function of temperature and is shown in Figure 21. Comparing with the experimental value from [51] at 1073 K, the calculated equilibrium volume is within 3%. Analyzing the slope of the volume versus temperature curve for the γ phase provides a volume coefficient of thermal expansion. A volume coefficient of thermal expansion is used as a comparison because this value is independent of the reference state chosen. The volume coefficient of thermal expansion of 0.19% per 100 K compares very well to the experimental value of 0.22% per 100 K [15].

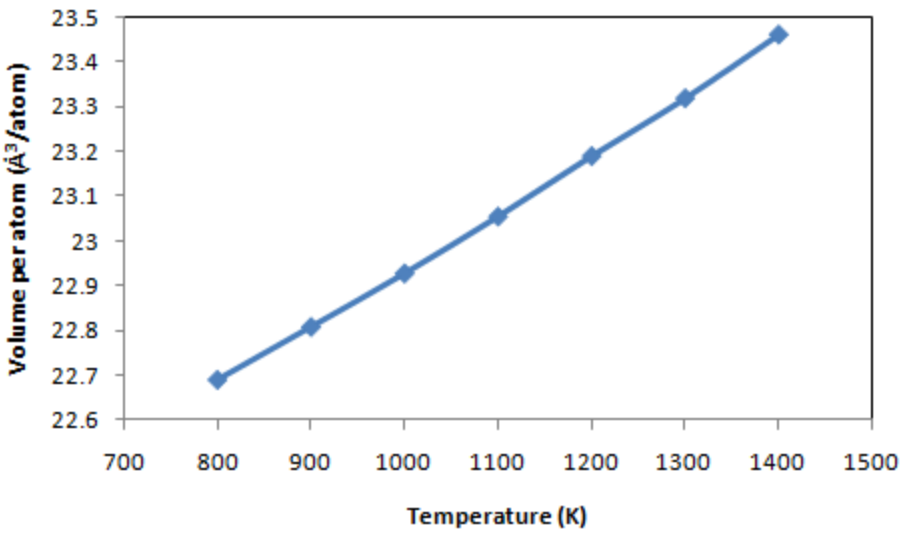


Figure 21. The equilibrium volume per atom ($Å^3$/at) as a function of temperature (K).

A summary of the melting temperature, enthalpy of fusion, volume change on melting, heat capacity and rate of thermal expansion is given in Table 12.

Table 12. The melting temperature, enthalpy of fusion, volume change on melting, specific heat capacity and thermal expansion are calculated and compared to experimental values [15, 64].

| | MEAM | Expt. |
|---|---|---|
| $T_{melt}$ (K) | 1410 | 1408[64] |
| $\Delta H_{fusion}$ (kJ/mol) | 8.66 | 8.5[64] |
| $\Delta V_{melt}$ (%) | 2.17 | - |
| $C_p$(J/g-K) | 0.11 | 0.12[64] |
| Volume Coefficient of Thermal Expansion (per 100 K) | 0.19% | 0.22% [15] |

**Self-Defect formation energy as a function of temperature**

In order to determine the defect formation energy in γ U, a single defect (vacancy or self-interstitial) was introduced into a relaxed 250 atom supercell and equilibrated for

10 ns (NVT). Average energies were computed over the final 5 ns. The vacancy formation energy was calculated from equation 2. The vacancy formation energy as a function of temperature is shown in Figure 22. The self-interstitial formation energy was calculated from equation 3. The self-interstitial is introduced as a <100> dumbbell. In the process of the simulation, the defect propagates throughout the system, changing orientations. Thus, the self-interstitial formation energy is an average over a variety of specific defect configurations. The self-interstitial formation energy as a function of temperature is shown in Figure 23.

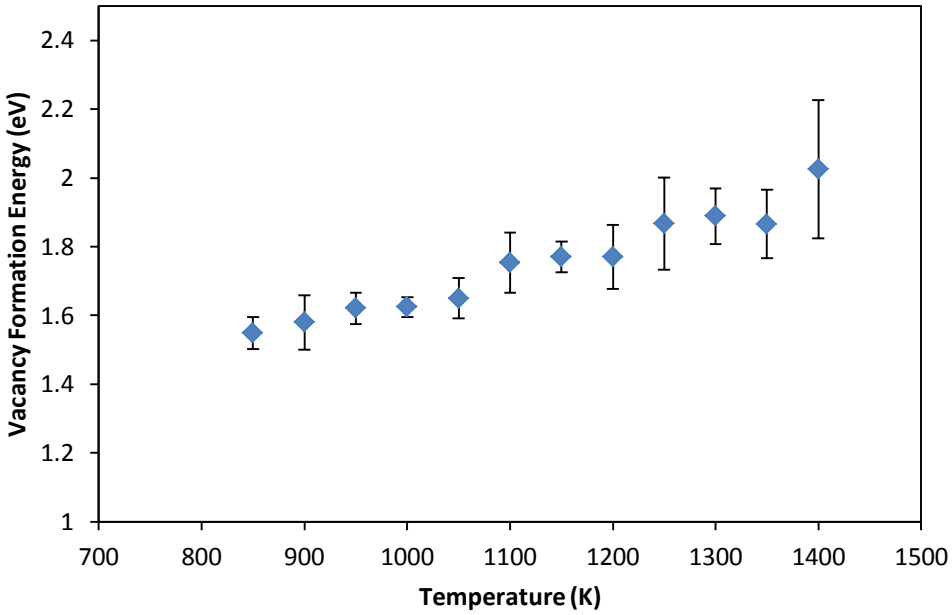


Figure 22. The vacancy formation energy in γ U as a function of temperature. Error bars represent a positive and negative standard error of the mean.

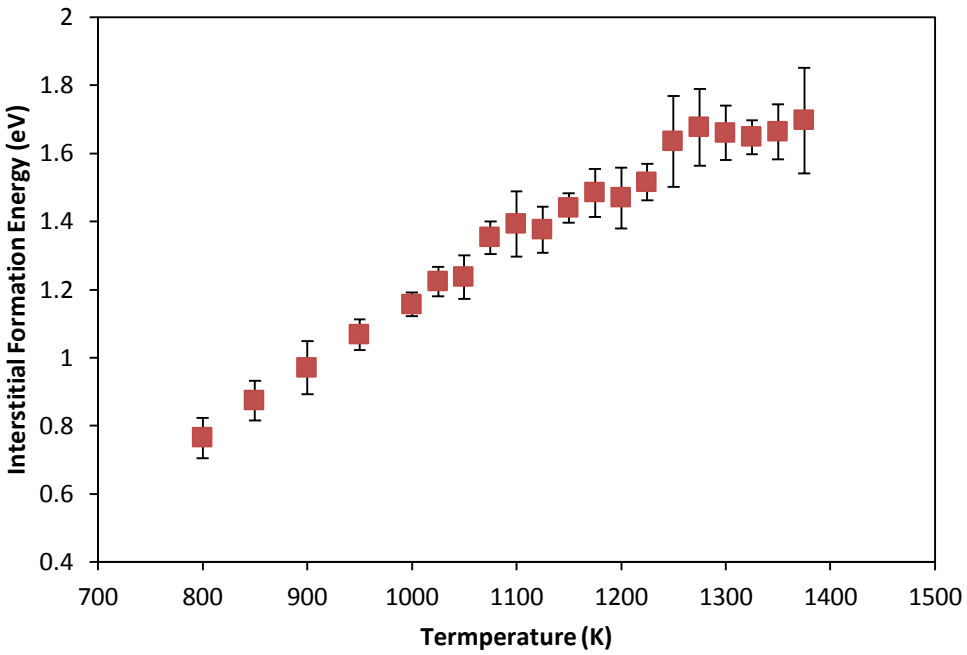


Figure 23. The self-interstitial formation energy in γ U as a function of temperature. Error bars represent a positive and negative standard error of the mean.

Figure 22 and Figure 23 show a strong dependence of the defect formation energy on temperature. From 800 K to 1400 K, the formation energy for a vacancy and a self-interstitial increases with increasing temperature, consistent with previous calculations in other systems [65-67] . Similar defect formation energy behavior has been seen in bcc Zr [67]. The magnitude of the vacancy formation energy at temperature is higher than as predicted at 0 K. The magnitude of the self-interstitial formation energy corresponds very well to previous computational work [68].

# CHAPTER 6

# BINARY MEAM INTERATOMIC POTENTIALS FOR γ U-HE, U-XE AND U-KR

## Molecular Statics Simulations

To perform molecular dynamics simulations on systems of uranium with a fission gas inclusion, a MEAM interaction description needs to be generated. The uranium-fission gas description implemented in this work was derived from first principles calculations. Point defects of He, Xe, and Kr in bcc uranium were calculated above, and theoretical intermetallic structures (B1, B2, and $L1_2$) were also investigated via DFT to develop cohesive energy relations between the two species. The equilibrium lattice parameter of each intermetallic, along with the energy of formation is presented in Table 13. The $L1_2$ crystal structure was stoichiometrically $U_3FG$. The energy of formation, $E_f$, is given by

$$E_f = E_{(U-FG)} - nE(U_\alpha) - mE\left(FG_{fcc}\right) \quad (26)$$

where $E_{(U\text{-}FG)}$ is the energy of an intermetallic unit cell, *n* is the number of uranium atoms present in the unit cell of the intermetallic, $E(U_\alpha)$ is the energy of a single uranium atom in the α phase, *m* is the number of fission gas atoms present in the unit cell of the intermetallic and $E(FG_{fcc})$ is the energy of a fission gas atom in the fcc phase.

Table 13. Equilibrium lattice parameters and formation energies for U-Xe, U-Kr and U-He theoretical intermetallic phases calculated with first principles DFT methods.

| | **B1** | | **B2** | | **$L1_2$** | |
|---|---|---|---|---|---|---|
| | $a_0$ (Å) | $E_f$ (eV) | $a_0$ (Å) | $E_f$ (eV) | $a_0$ (Å) | $E_f$ (eV) |
| **UXe** | 6.271 | 5.285 | 3.967 | 5.088 | 4.497 | 6.630 |
| **UKr** | 6.065 | 5.397 | 4.158 | 5.176 | 4.437 | 6.757 |
| **UHe** | 5.191 | 3.355 | 3.148 | 3.624 | 4.133 | 4.459 |

Table 14. MEAM parameters for a bcc uranium-fission gas potential. Sources for the parameters are from experiment and from density functional theory calculations. For the binary systems the screening parameters for screening of two uranium atoms by the fission gas atom is given. All other screening parameters were taken as $C_{min}$=2.8 and $C_{min}$=2.0.

| **Parameter** | **U** | **He** | **Xe** | **Kr** | **U-He** | **U-Xe** | **U-Kr** |
|---|---|---|---|---|---|---|---|
| *Reference Structure* | fcc | diatomic | fcc | fcc | diatomic | B1 | B1 |
| $E_c$ (eV) | 5.27 | 0.0005 | 0.032 | 0.035 | 0.005 | 1.0 | 0.1 |
| $r_e$ (Å) | 3.083 | 2.96 | 4.90 | 4.384 | 3.7 | 3.042 | 3.025 |
| $\alpha_i$ | 5.1 | 7.6 | 7.8 | 8.7 | 7.0 | 8.0 | 13.1 |
| $\delta$ | 0.1 | 0 | 0 | 0 | 0 | 0.2 | 0.2 |
| $A_i$ | 1.04 | 0.15 | 0 | 1 | - | - | - |
| $\beta^{(0)}$ | 6.0 | 9.1 | 7 | 8.7 | - | - | - |
| $\beta^{(1)}$ | 6.8 | - | - | - | - | - | - |
| $\beta^{(2)}$ | 7.0 | - | - | - | - | - | - |
| $\beta^{(3)}$ | 7.0 | - | - | - | - | - | - |
| $t^{(0)}$ | 1 | 1 | 1 | 1 | - | - | - |
| $t^{(1)}$ | 2.5 | 0 | 0 | 0 | - | - | - |
| $t^{(2)}$ | 4 | 0 | 0 | 0 | - | - | - |
| $t^{(3)}$ | 3 | 0 | 0 | 0 | - | - | - |
| $\rho_0$ | 1 | 0.022 | 0.045 | 0.162 | - | - | - |
| $C_{max}$ | 1.7 | 2.8 | 2.8 | 2.8 | 0.4 | 1.8 | 2.8 |
| $C_{min}$ | 1.2 | 2.0 | 2.0 | 2.0 | 0.1 | 0.2 | 0.2 |

This work using density functional theory provides an adequate basis for the development of uranium-fission gas MEAM models. The fission gas MEAM potential parameters are given in Table 14 for the three fission gases studied. Using these calculated interatomic potentials for u-fission gas systems, the formation energy of fission gas point defects is calculated via inserting a fission gas defect into an ideal system with equilibrium lattice constants [60]. The defect formation energies were calculated from equations 6 and 7. The formation energies of point defects in bcc

uranium of He, Xe, and Kr are displayed in figures 24-26, respectively, and presented in tables 15-17.

Table 15. Formation energies (eV) of helium point defects in bcc uranium calculated via density functional theory and using a MEAM potential.

| | MEAM | DFT |
|---|---|---|
| substitutional | 1.842 | 1.803 |
| <100> | 3.026 | 2.234 |
| <110> | 3.120 | 2.148 |
| <111> | 3.901 | 1.764 |
| tetrahedral | 3.051 | 2.434 |

Table 16. Formation energies (eV) of xenon point defects in bcc uranium calculated via density functional theory and using a MEAM potential.

| | MEAM | DFT |
|---|---|---|
| substitutional | 5.376 | 5.549 |
| <100> | 9.482 | 7.294 |
| <110> | 11.988 | 7.037 |
| <111> | 18.153 | 10.085 |

Table 17. Formation energies (eV) of krypton point defects in bcc uranium calculated via density functional theory and using a MEAM potential.

| | MEAM | DFT |
|---|---|---|
| substitutional | 5.116 | 5.926 |
| <100> | 6.049 | 6.549 |
| <110> | 8.067 | 7.345 |
| <111> | 15.227 | 8.420 |

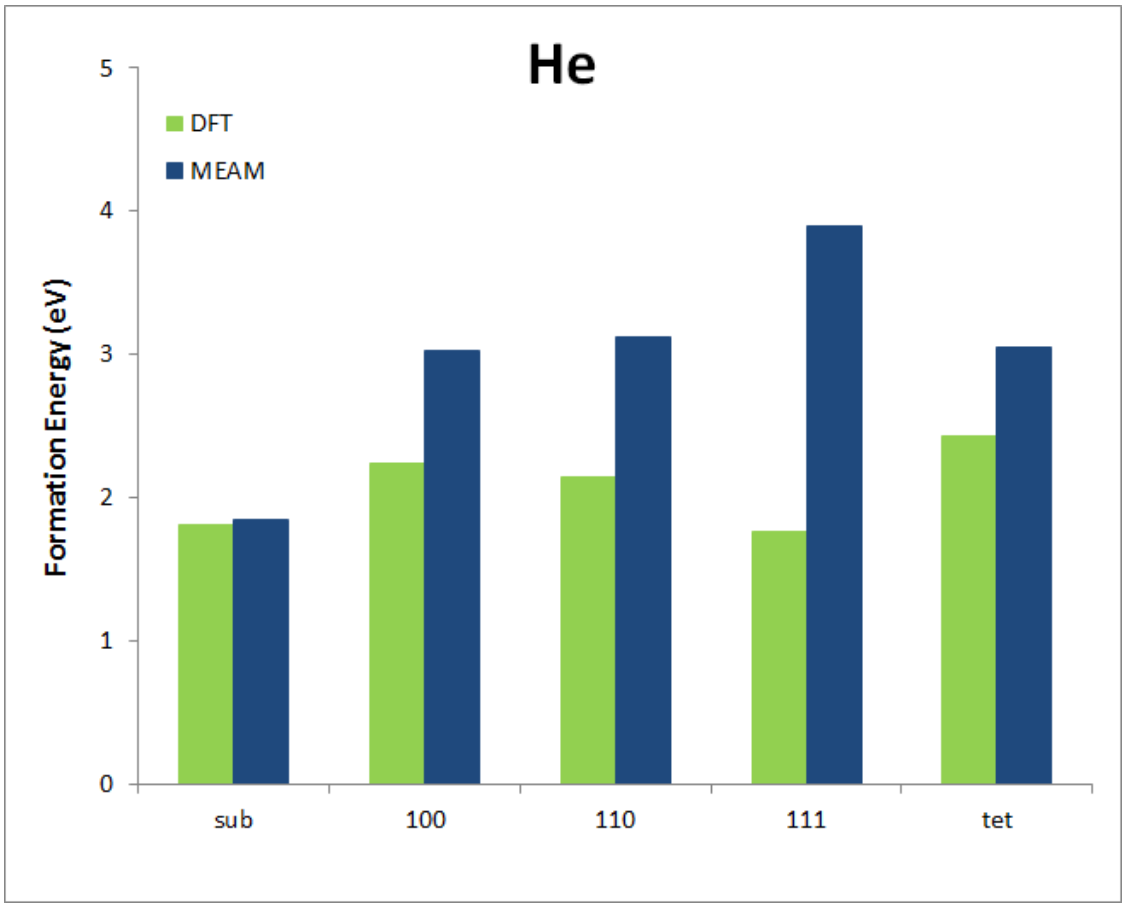


Figure 24. Formation energies (eV) of helium point defects in bcc uranium calculated via density functional theory and using a MEAM potential. During the molecular statics energy minimization, the octahedral interstitial relaxed to an <100> dumbbell interstitial.

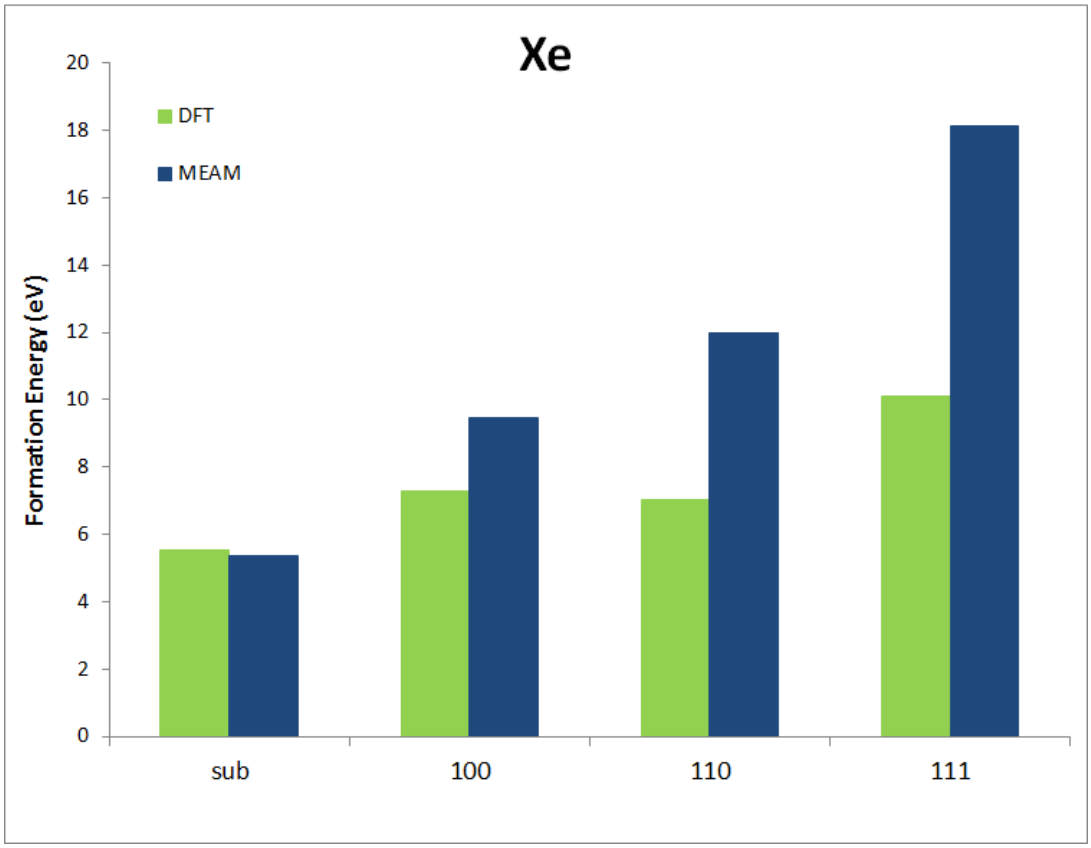


Figure 25. Formation energies (eV) of xenon point defects in bcc uranium calculated via density functional theory and using a MEAM potential. During the molecular statics energy minimization, the octahedral and tetrahedral interstitials relaxed to an <100> dumbbell interstitial.

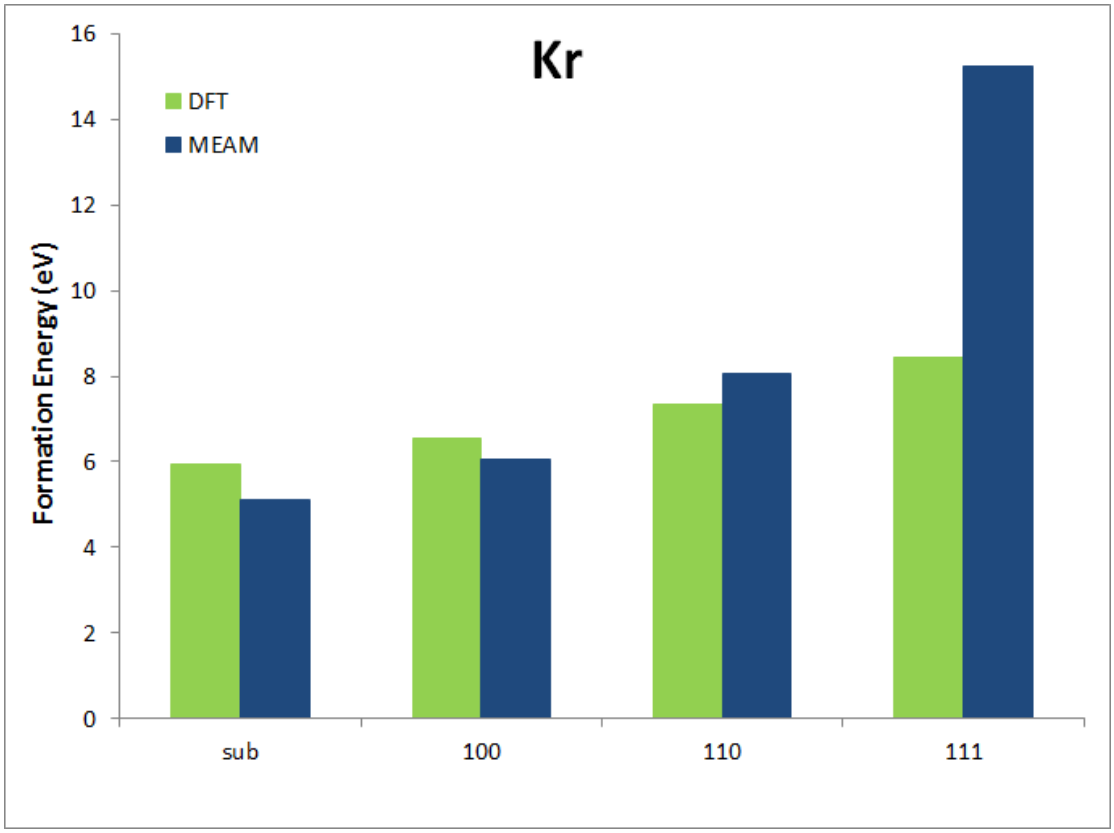


Figure 26. Formation energies (eV) of krypton point defects in bcc uranium calculated via density functional theory and using a MEAM potential. During the molecular statics energy minimization, the octahedral and tetrahedral interstitials relaxed to an <100> dumbbell interstitial.

Excellent agreement is seen between the MEAM potentials and the DFT results. There exists a size effect, in that the species with the smallest atomic radius (He) has the lowest formation energies and Xe and Kr with much larger atomic radii have approximately equal formation energies. This is in agreement with DFT work above. Helium is likely to be found in a wide variety of defect configurations, while Xe and Kr are likely to be present as substitutionals. It is interesting to note that some defects undergo a reconfiguration during the molecular statics energy minimization. For He, the

octahedral interstitial becomes a <100> dumbbell interstitial. For Xe, the octahedral and tetrahedral interstitials become a <100> dumbbell. For Kr, the octahedral and tetrahedral interstitials become a <100> dumbbell. For all reconfiguration of defects, DFT results show less than a 0.3 eV variance between the formation energies of the initial and final defect configurations. For some systems of defects, particularly the <111> dumbbell, there is a relatively large overestimation of the defect formation energy. This is due to inherent short interatomic distances incurred in the calculation of point defects and the differences between the short-range potential description for the pseudopotentials utilized in DFT work above and the MEAM interatomic potentials utilized in this work. If a larger shell was implemented in these calculations, allowing further relaxation and typically larger interatomic spacing within a defect, the converged formation energy would approach that calculated via DFT. In general, the results from molecular statics agree very well with the DFT calculations.

## Molecular Dynamics Simulations

In this dissertation, molecular dynamics investigations will only be presented for pure uranium and the binary uranium-xenon systems.

### Void Energetics

In nuclear reactor fuels, fission gases most often exist as bubbles [1], the formation of which is aided by vacancy diffusion and clustering. Thus, in order to begin understanding how fission gases interact within a system of uranium, the properties of multiple vacancy systems and vacancy clusters must be investigated. To study the energetics of vacancy clustering, a 16000 atom supercell was equilibrated at a given

temperature. A sphere of atoms was then removed in the center of the supercell and this system was allowed to relax. This was performed from 800 K to 1200 K in increments of 100 K. The results of these calculations at 800 K are shown in Figure 27 and compared with an extrapolated monovacancy formation energy. The data is shown for a system with up to twenty vacancies. The data points for clustered vacancies exhibit lower formation energies than isolated vacancies. A lower formation energy for a clustered vacancy system shows evidence of vacancy binding and preferential clustering, as it is more energetically favorable for vacancies to be nearest neighbors. It is interesting to note that below a cluster of 12 vacancies, the single spherical void introduced into the system dissociates into multiple vacancy clusters. The clusters remain bound to one another; however, the presence of a single void is less energetically favorable than multiple small clusters of vacancies. Above 12 vacancies, a singular void is more energetically favorable than multiple vacancy clusters due to contributions from the surface energy of the void(s).

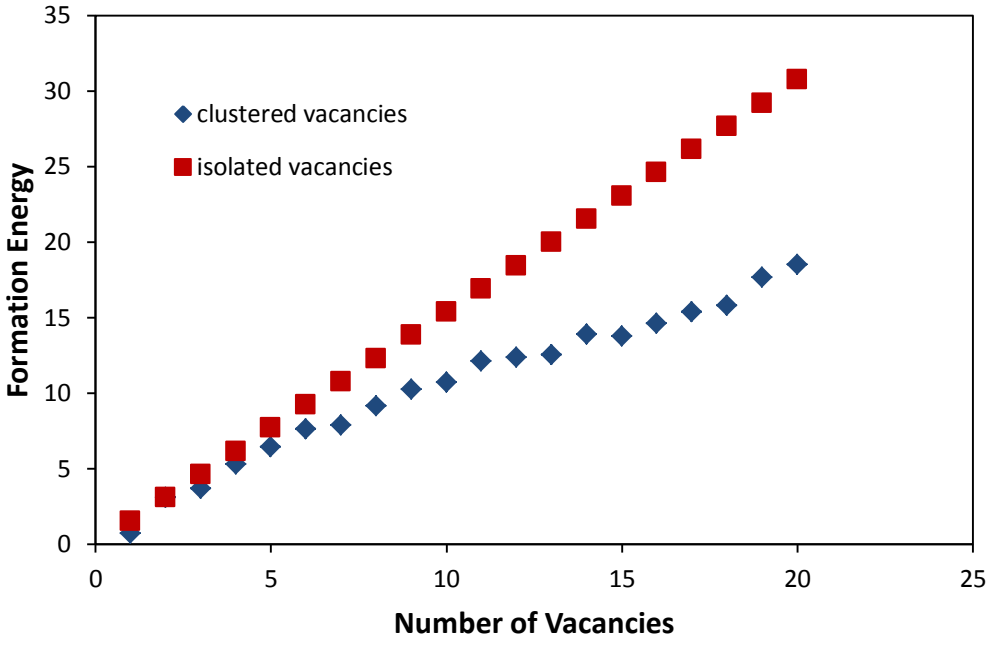


Figure 27. Formation energy of a multiple vacancy systems as a function of the number of vacancies within that system at 800 K. Red squares are extrapolated monovacancy formation energy. Blue diamonds are the energy of clustered vacancies. Lower formation energies for clustered vacancies shows evidence of vacancy binding and preferential clustering.

Analyzing larger clusters of vacancies can yield a more general picture of vacancy behavior. In Figure 28, the formation energy is displayed for vacancy clusters up to approximately 650 vacancies, equivalent to a void with a diameter of 3 nm. This information is displayed for temperatures from 800 K to 1200 K. It is seen that for all temperatures a power law is exhibited for the formation energy of a void as a function of the number of vacancies composing that void. The slope slightly decreases as the temperature increases. This leads to stronger binding of vacancies as the temperature increases. The binding energy of the $n^{th}$ vacancy in a void of n vacancies is defined by :

$$BE = E_f(n-1) + E_f(1) - E_f(n) \quad (27)$$

where BE is the binding energy, $E_f$(n-1) is the formation energy of a void comprised of (n-1) vacancies, $E_f$(1) is the monovacancy formation energy and $E_f$(n) is the formation energy of a void comprised of *n* vacancies. Given that the behavior of the formation energy of a void as a function of the number of vacancies within that void displays a power law relationship, it is clear that as the void size increases, the $n^{th}$ vacancy becomes progressively more tightly bound. An examination of the $n^{th}$ vacancy for a void smaller than 100 vacancies reveals the binding energy is approximately 1 eV. For voids of size 100 vacancies to 650 vacancies, the binding energy of the $n^{th}$ vacancy is approximately 1.2 eV. As a point of note, these relationships are not intended to describe void behavior outside of the ranges of void sizes investigated.

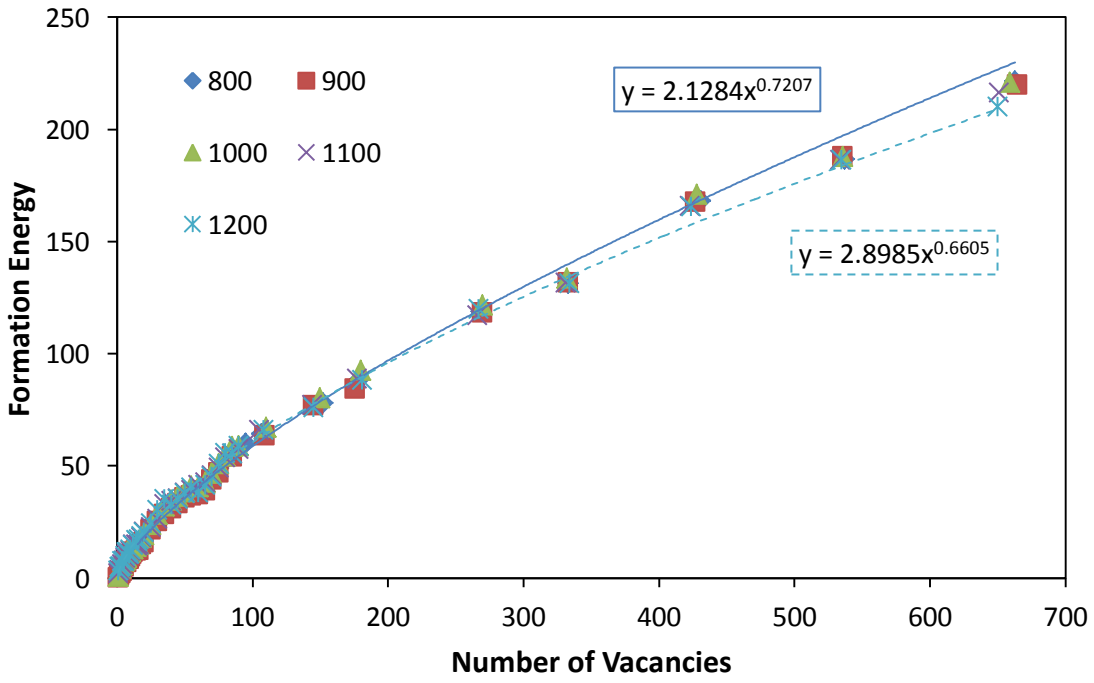

Figure 28. Formation energy of a multiple vacancy systems as a function of the number of vacancies within that system from 800 K to 1200 K. A power law relationship is observed for the formation energy of a void as a function of the number of vacancies. Formation energy slightly decreases with increasing temperature, indicating stronger vacancy binding as temperature increases. Fits to data are only shown for 800 K and 1200 K, with solid and dashed lines respectively.

Finally, the amount of swelling as a function of the void size is calculated from:

$$\frac{\Delta V}{V_0} = \frac{V_{system} + n_{vac} * V_{atom}}{V_0} \quad (28)$$

where $V_{system}$ is the volume of the system with *n* vacancies, $n_{vac}$ is the number of vacancies in the system, $V_{atom}$ is the volume per atom in an pure equilibrated system and $V_0$ is the volume of the pure system with no vacancies. This equation for swelling makes the assumption that atoms removed to create vacancies are moved to the bulk, with an associated equilibrium volume per atom. The results for swelling calculations are displayed for 800 K in Figure 29. The swelling percent is linear as a function of the number of vacancies in a void. This linear behavior holds for all temperatures analyzed.

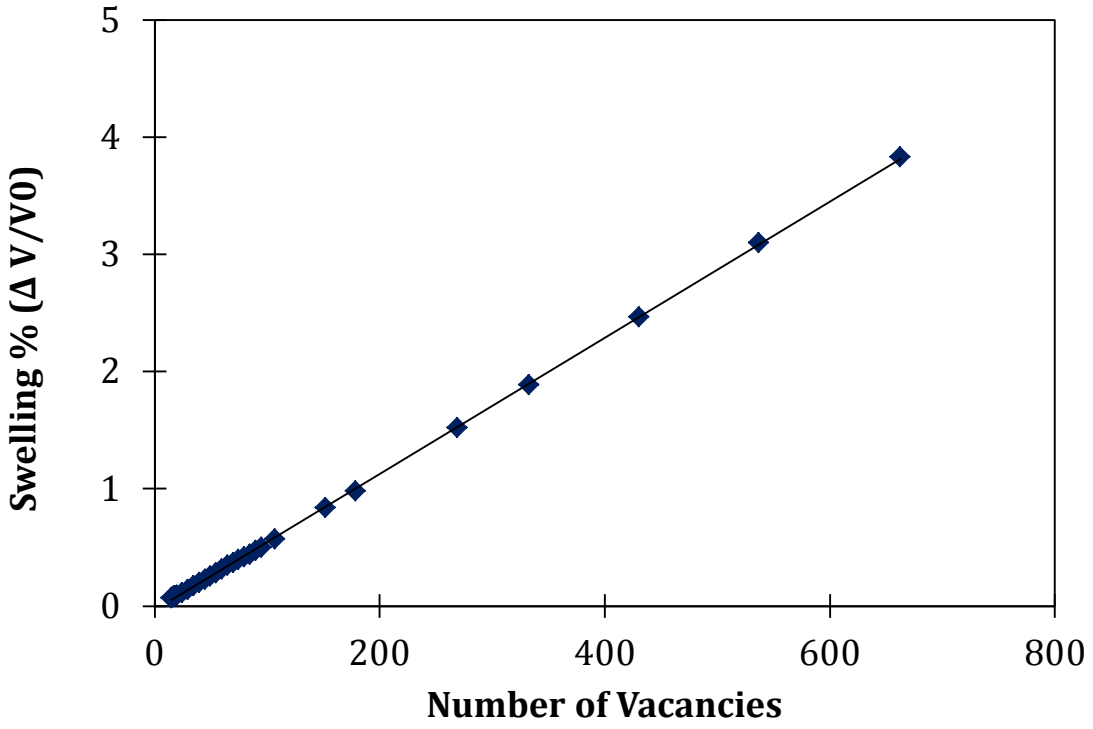


Figure 29. Swelling percent as a function of the number of vacancies comprising a single void at 800 K. A linear relationship is observed for the entire range of void sizes analyzed. This linear behavior holds for all temperatures.

**Xenon Bubble Energetics**

Given void energetics, the effects of fission gases on system energy and on swelling can be analyzed. Initially, Xe behavior as a dilute substitutional defect should be investigated, to gain information on general point defect behavior related to temperature. In Figure 30, the substitutional defect formation is displayed as a function of temperature. Slightly positive linear behavior is observed as a function of temperature. Thus, very little change in substitutional formation energy is observed for the entire range of temperatures analyzed. Error bars are standard error of the mean, averaged over eight simulations of a pure system and summed with an average over eight simulations of a system including a defect.

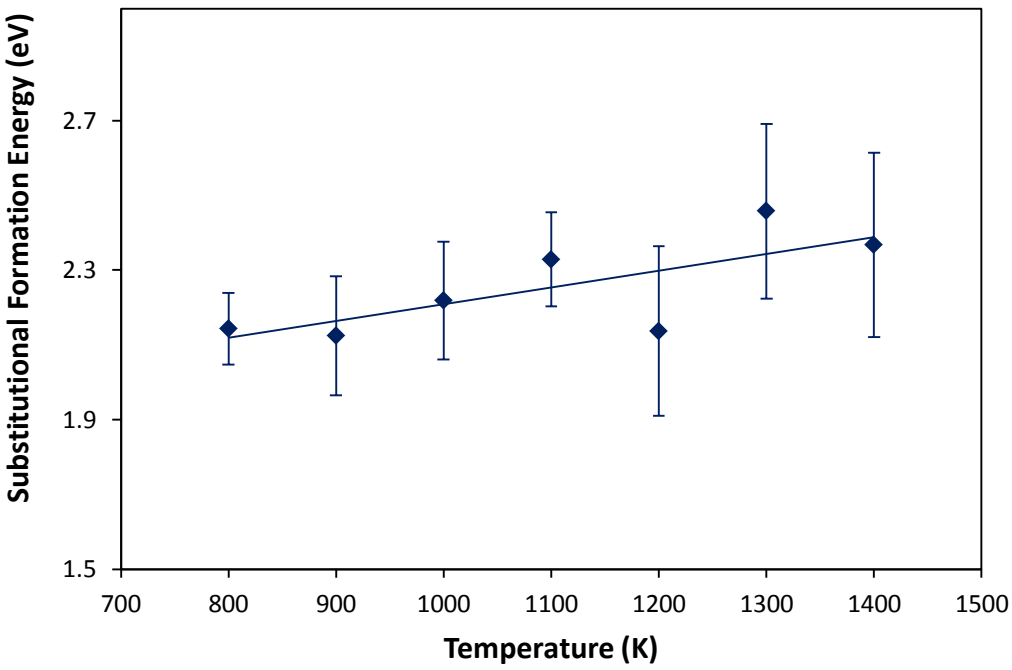


Figure 30. Xenon substitutional formation energy as a function of temperature. Slightly positive linear slope is observed with respect to temperature. Error bars are standard error of the mean.

Xenon bubbles can be investigated by utilizing the study of voids completed above. Starting with a relaxed void of a given number of vacancies, xenon atoms are incrementally added into the void, creating a bubble. The formation energy and volume are determined after each incremental addition of xenon atoms. Xenon atoms are continually introduced until the inclusion of one additional xenon atom within the bubble produces a self-interstitial within the bulk. The results for the formation energy as a function of the number of Xe atoms within a void comprised of 90 vacancies are displayed in Figure 31. It is observed that initially, as Xe atoms are introduced into the bubble, minimal changes are observed in the formation energy. Thus, addition of xenon atoms yields no appreciable increase in the formation energy of the bubble, stating that it

is very energetically favorable for Xe atoms to reside in a bubble, as opposed to Xe atoms residing as substitutionals in the bulk. In Figure 31, this behavior is exhibited up to approximately 40 Xe atoms. In this region, the slope of the formation energy as a function of Xe atoms is linear and zero. As progressively more Xe atoms are added into the bubble, the formation energy displays an exponential growth relationship with regards to the number of Xe atoms. Thus, although it is still energetically favorable for Xe atoms to reside in a bubble, there is a non-negligible increase in the energy of the system.

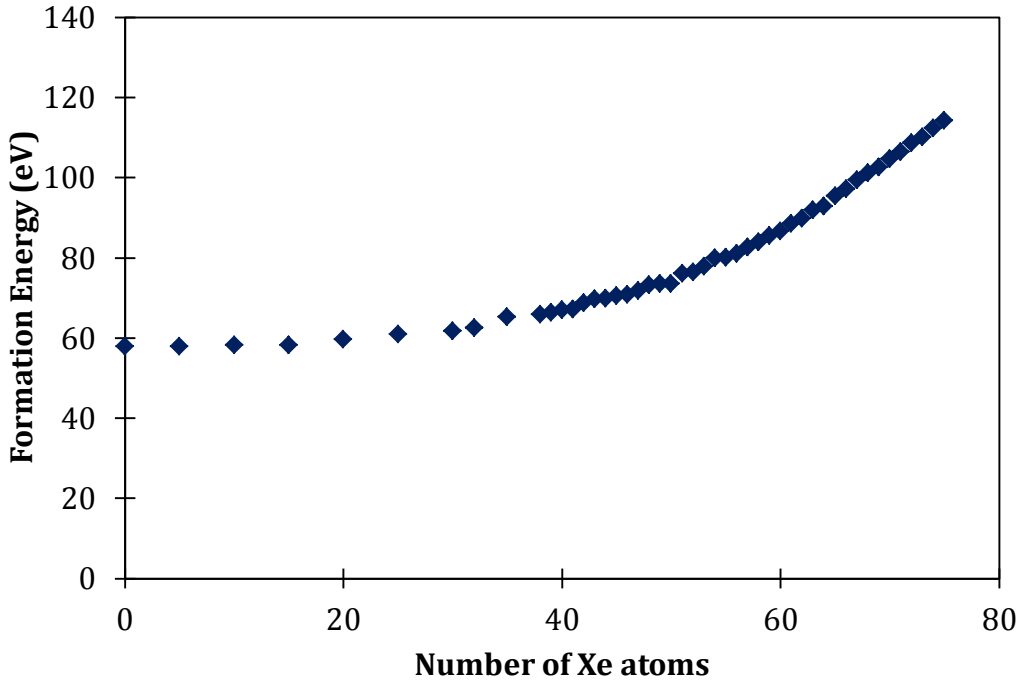


Figure 31. Formation energy of a xenon bubble as a function of the number of xenon atoms present within the bubble. The bubble is comprised of 90 vacancies.

Volume was also analyzed as a function of the number of Xe atoms added into a void of 90 vacancies. The results from these calculations are displayed in Figure 32. Initially, as Xe atoms are added into the bubble, there is a minimal linear increase in

volume as a function of the number of Xe atoms. Again, behavior changes above approximately 40 Xe atoms, and swelling displays exponential growth behavior as a function of the number of Xe atoms within the bubble.

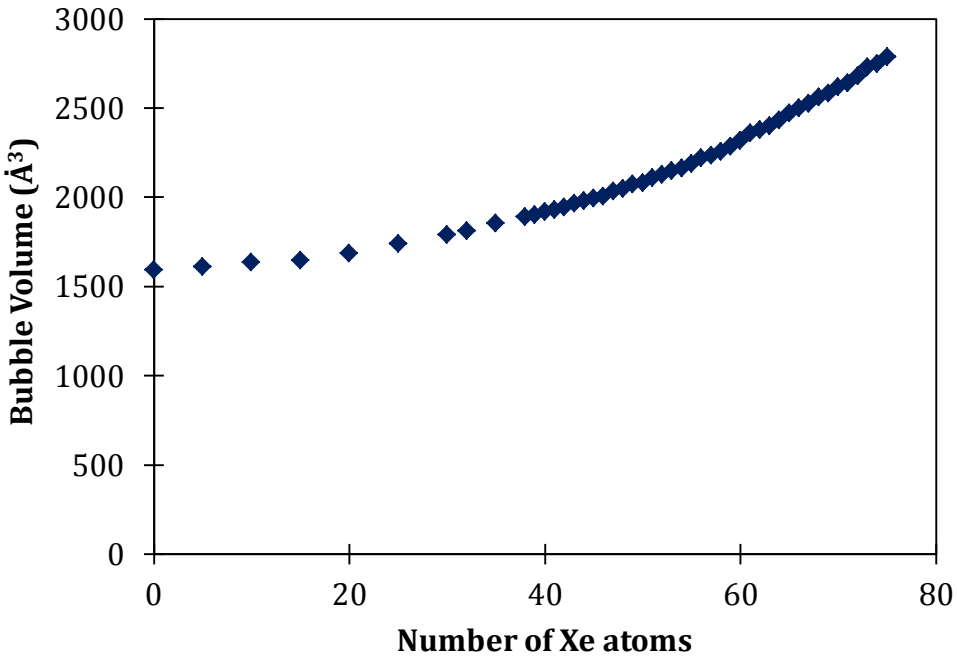


Figure 32. Bubble volume as a function of the number of Xe atoms within the bubble. The bubble is comprised of 90 vacancies.

Atoms of Xe are incrementally added into the bubble until a self-interstitial is created and ejected into the bulk lattice. The maximum number of Xe atoms that can be inserted into a bubble before creation of self-interstitials is displayed in Figure 33. This was calculated for voids consisting of fewer than 100 vacancies, analogous to voids with a diameter less than 1.5 nm. There exists a general linear dependence for the maximum number of Xe atoms that can be inserted into a void of a given size. The slope of this linear dependence is 0.8857, as displayed in Figure 33. Thus, given a void size, the

maximum number of Xe atoms that can be inserted into a void before a self-interstitial is ejected is approximately 90% of the number of vacancies comprising the particular void of interest.

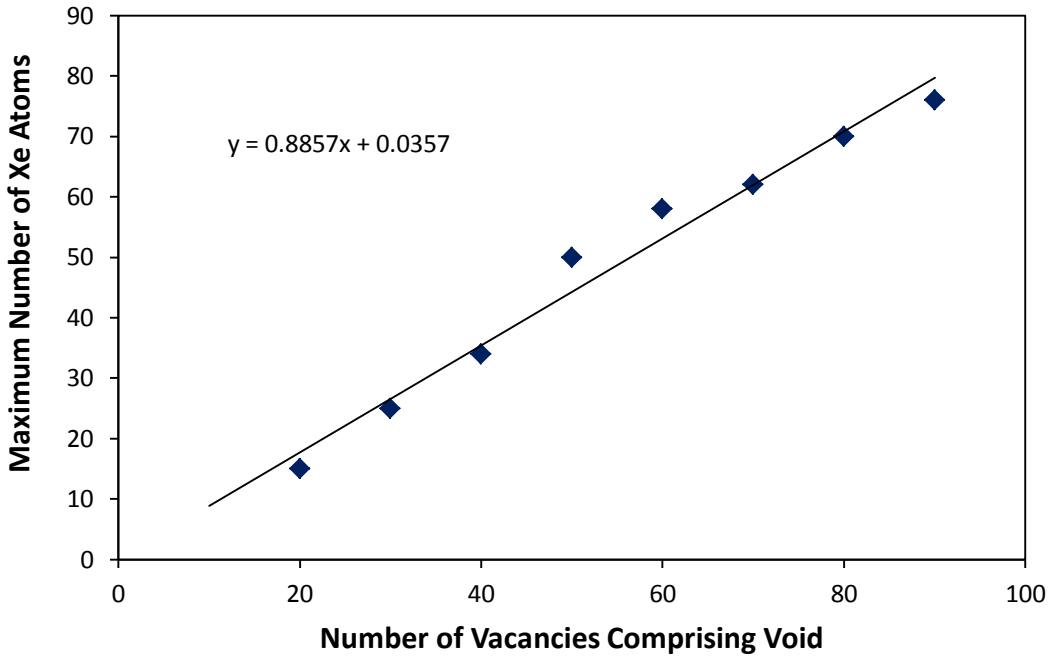


Figure 33. The maximum number of xenon atoms that can be inserted in a void of a given size without the creation of a self-interstitial atom. Regardless of void size, the maximum number of Xe atoms that can be inserted in a void is approximately 90% of the number of vacancies that constitute a given void.

**Xenon effect on vacancy self-diffusion**

Xenon also impacts the bulk system of uranium with regards to diffusion of point defects. The primary means of self-diffusion in uranium is theorized to be mediated by vacancies [15], and there exists a non-zero attractive force between xenon substitutional atoms and vacancies. A xenon substitutional atom existing as a nearest neighbor to a vacancy reduces the overall lattice strain produced by the two defects. Lattice strain is

higher in systems where vacancies and xenon atoms are isolated, thus, the energy of the system is higher. To demonstrate this effect, DFT calculations were performed on 54 atom bcc supercells containing a vacancy and a xenon substitutional, following computational procedures outlined previously. The energy of the two defects isolated in the bulk is calculated and compared with the energy of the system when the vacancy and xenon substitutional are neighbors. The energy difference of nearest neighbor (NN) configurations with respect to isolated bulk defects is presented in Figure 34. It is seen that as first nearest neighbors (1NN), the energy of the system is reduced by approximately 1 eV, compared with isolated bulk defects. The energy difference decreases with increasing distance between the xenon substitutional and the vacancy. For a distance of fourth nearest neighbors (4NN), the energy difference compared to the isolated bulk defects is zero. Thus, there is a short range attractive interaction between vacancies and xenon substitutionals with a maximum attractive energy of approximately 1 eV.

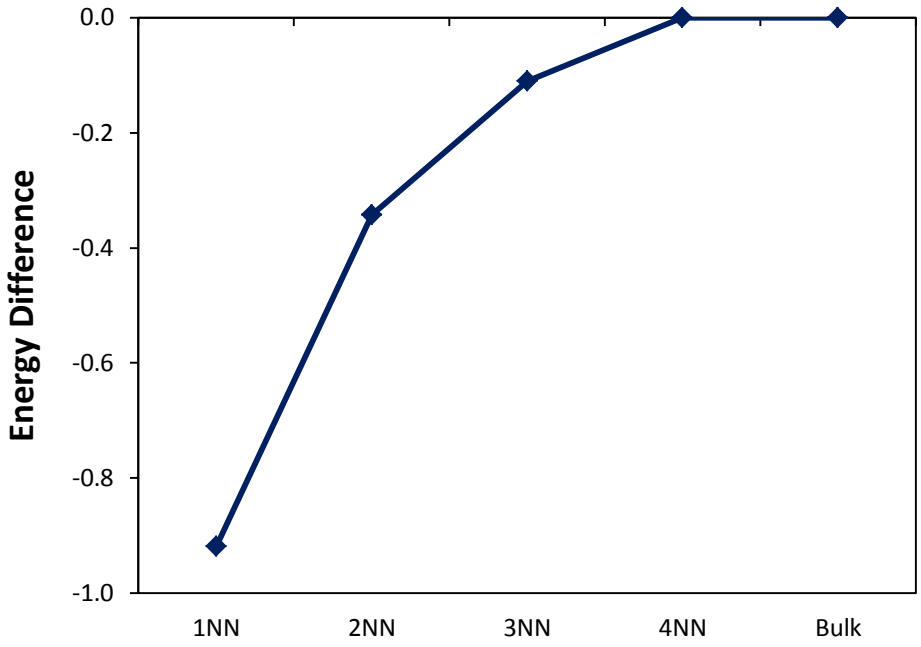


Figure 34. The energy difference of nearest neighbor configurations of a vacancy and a Xe substitutional with respect to defects isolated in the bulk. The maximum energy difference occurs for first nearest neighbors (1NN), with a magnitude of approximately 1 eV. The energy of the system is reduced when a Xe substitutional and a vacancy are neighbors.

The attractive effect is not as simple to calculate at temperature, due to diffusion of vacancies. Thus, the attractive effect can be interpreted via the impact of xenon substitutionals on the self-diffusion of uranium via a vacancy mechanism. Two systems of 250 atoms were equilibrated and initialized. One system contained a vacancy and a Xe substitutional atom randomly inserted into the lattice. One system contained only a vacancy randomly inserted into the lattice. The system was allowed to evolve for 50 ns, allowing diffusion of vacancies and ensuring that random walk diffusion would result in interaction of a vacancy with a Xe substitutional. The average mean square displacement

(msd) over all uranium atoms is calculated as a function of time. The msd for the Xe substitutional is also calculated and determined to be zero in all simulations. Thus, on the time scale analyzed, Xe substitutionals are immobile. This work was performed for temperatures from 800 K to 1400 K, in increments of 100 K. Selected results are displayed in figures 35-38.

Figure 35 displays the msd as a function of time at 800 K for a system containing a single vacancy, and a system containing a single vacancy with a Xe substitutional. For a monovacancy, general linear behavior as a function of time is observed, as would be expected. For the system containing a Xe substitutional, linear behavior as a function of time is NOT observed. Instead, the msd displays a plateauing behavior as a function of time. This is evidence that the vacancy is diffusing through the bulk, interacts with the Xe atom, and experiences a pseudo-pinning effect, limiting further diffusion of the vacancy. This is confirmed on visual examination of the systems, which shows the vacancy and Xe substitutional in close proximity at the end of the simulation and throughout the plateaued region.

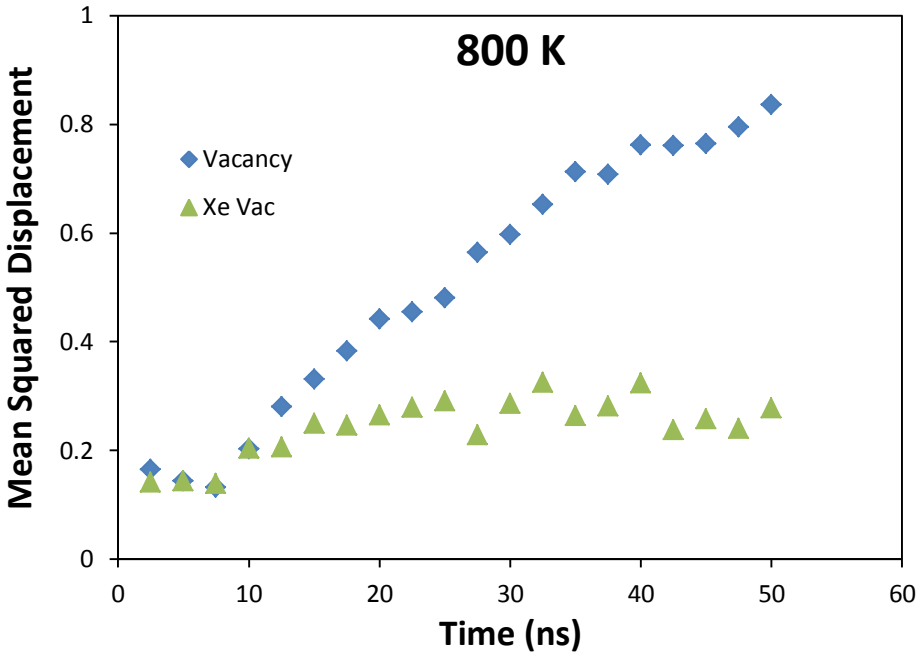


Figure 35. Mean squared displacement of monovacancy systems as a function of time at 800 K. Blue diamonds denote mean square displacement of uranium atoms with a single vacancy. Green triangles denote mean square displacement of uranium atoms with a single vacancy and xenon substitutional.

Figure 36 displays the msd as a function of time at 900 K for a system containing a single vacancy, and a system containing a single vacancy with a Xe substitutional. For a monovacancy, general linear behavior as a function of time is observed, as would be expected. For the system containing a Xe substitutional, linear behavior as a function of time is again NOT observed. Instead, the msd displays a plateauing behavior as a function of time. The plateauing region begins at approximately 25 ns, much later than is observed at 800 K. This can be explained as partially random, due to the random walk of the vacancy, and partially due to thermal fluctuations being strong enough to overcome the vacancy-Xe attraction.

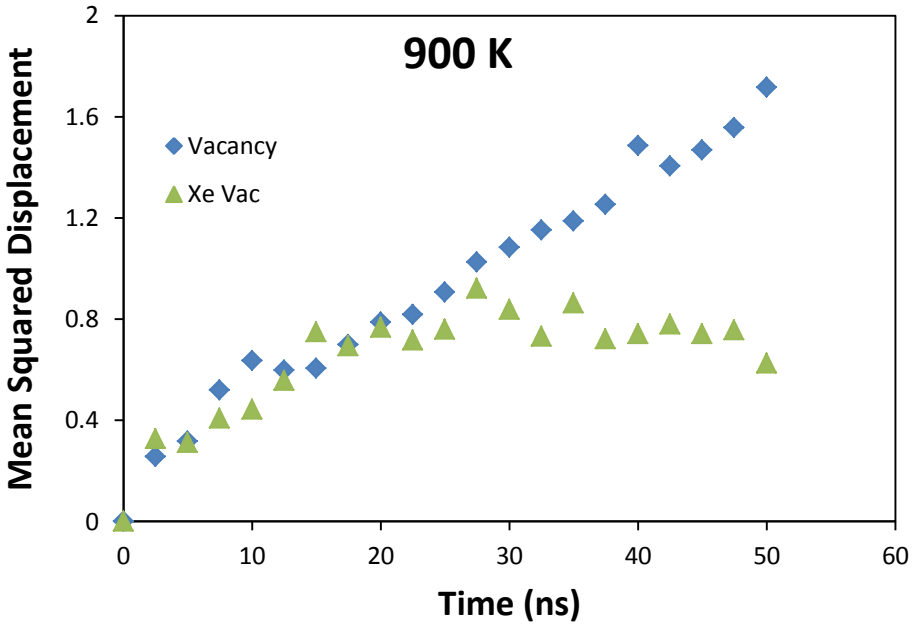


Figure 36. Mean squared displacement of monovacancy systems as a function of time at 900 K. Blue diamonds denote mean square displacement of uranium atoms with a single vacancy. Green triangles denote mean square displacement of uranium atoms with a single vacancy and a xenon substitutional.

Figure 37 displays the msd as a function of time at 1100 K for a system containing a single vacancy, and a system containing a single vacancy with a Xe substitutional. For a monovacancy, general linear behavior as a function of time is observed, as would be expected. For the system containing a Xe substitutional, linear behavior as a function of time is also observed. At this higher temperature, thermal fluctuations are strong enough to overcome any attractive forces between the vacancy and the Xe substitutional. Thus, a Xe substitutional produces no measurable effect on the diffusion of vacancies at 1100 K.

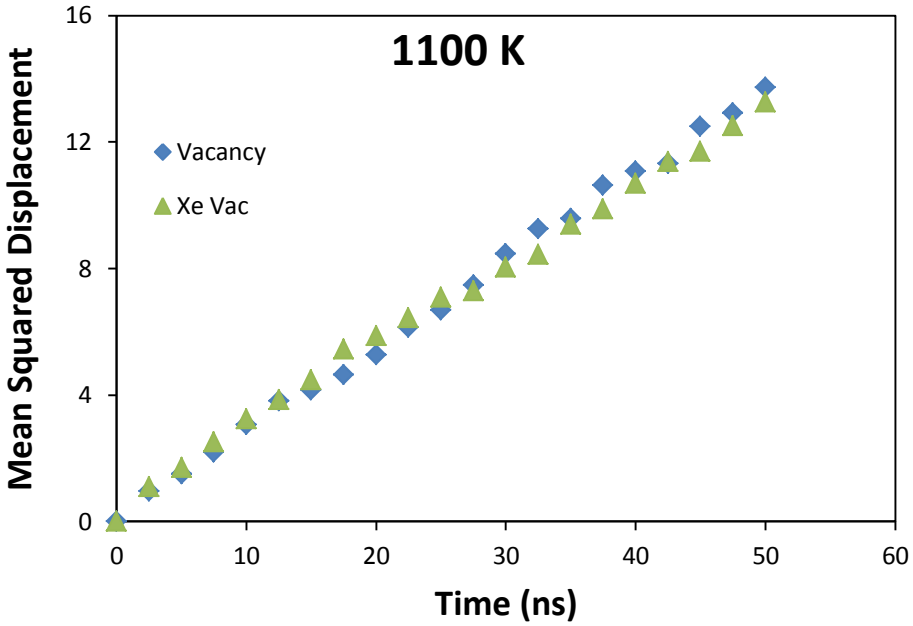


Figure 37. Mean squared displacement of monovacancy systems as a function of time at 1100 K. Blue diamonds denote mean square displacement of uranium atoms with a single vacancy. Green triangles denote mean square displacement of uranium atoms with a single vacancy and a xenon substitutional.

Figure 38 displays the msd as a function of time at 1300 K for a system containing a single vacancy, and a system containing a single vacancy with a Xe substitutional. For a both systems, general linear behavior as a function of time is observed. Similar to behavior at 1100 K, the presence of a Xe substitutional atom engenders no significant impact on the vacancy diffusion. Thus, thermal fluctuations are strong enough to overcome attractive forces between the vacancy and the Xe substitutional.

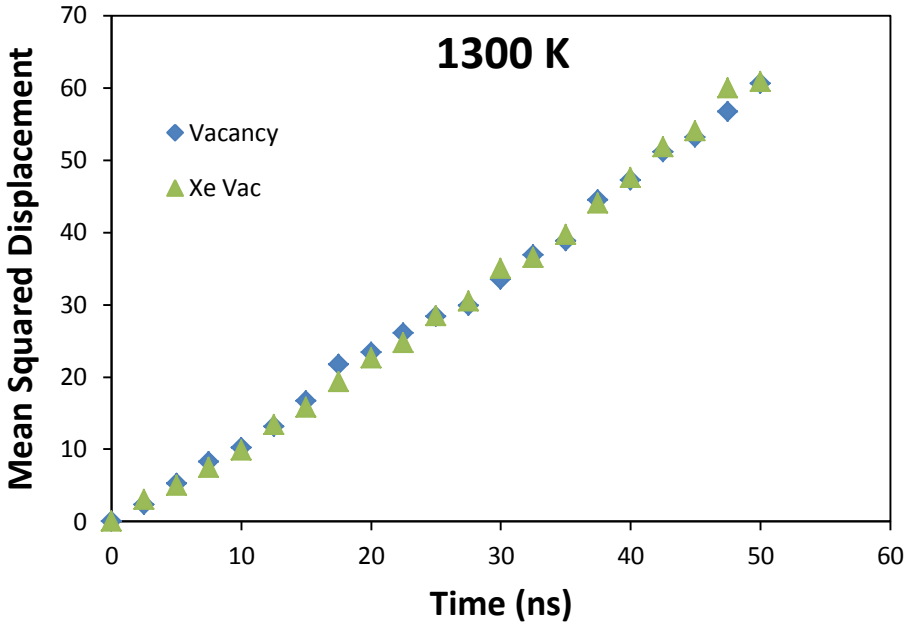


Figure 38. Mean squared displacement of monovacancy systems as a function of time at 1300 K. Blue diamonds denote mean square displacement of uranium atoms with a single vacancy. Green triangles denote mean square displacement of uranium atoms with a single vacancy and a xenon substitutional.

In addition to investigating the effect of Xe on diffusion of a single vacancy, it is of interest to examine Xe effects on systems containing multiple vacancies. Two systems of 250 atoms were equilibrated and initialized. One system contained four vacancies and a Xe substitutional atom randomly inserted into the lattice. One system contained only four vacancies randomly inserted into the lattice. The system was allowed to evolve for 50 ns, allowing diffusion of vacancies and ensuring that random walk diffusion would result in the interaction of vacancies with each other as well as vacancy interaction with the Xe substitutional. The average mean square displacement (msd) over all uranium atoms is calculated as a function of time [66]. The msd for the Xe substitutional is also

calculated and determined to be zero in all simulations. Thus, on the time scale analyzed, Xe substitutionals are immobile. This work was performed for temperatures from 800 K to 1400 K, in increments of 100 K. Selected results are displayed in figures 39-42.

Figure 39 displays the msd as a function of time at 800 K for a system containing four vacancies, and a system containing four vacancies with a Xe substitutional. For the system with only four vacancies, general linear behavior as a function of time is observed initially. After approximately 20 ns, the msd exhibits a plateauing behavior. This data is an expression of vacancy clustering, and the vacancy cluster acting as a pinning site for vacancies. Vacancies are clustering, and the energetic attraction between the vacancies themselves is strong enough such that diffusion is inhibited. For the system containing a Xe substitutional, the plateauing behavior occurs much earlier and results in a much lower value of the msd. Thus, vacancies are diffusing through the bulk, finding the Xe substitutional, clustering and experiencing a pseudo-pinning effect, limiting further diffusion of the vacancy. The presence of a Xe substitutional exacerbates the inherent tendency of vacancies to cluster and thus exacerbates the suppression of vacancy diffusion via vacancy pinning.

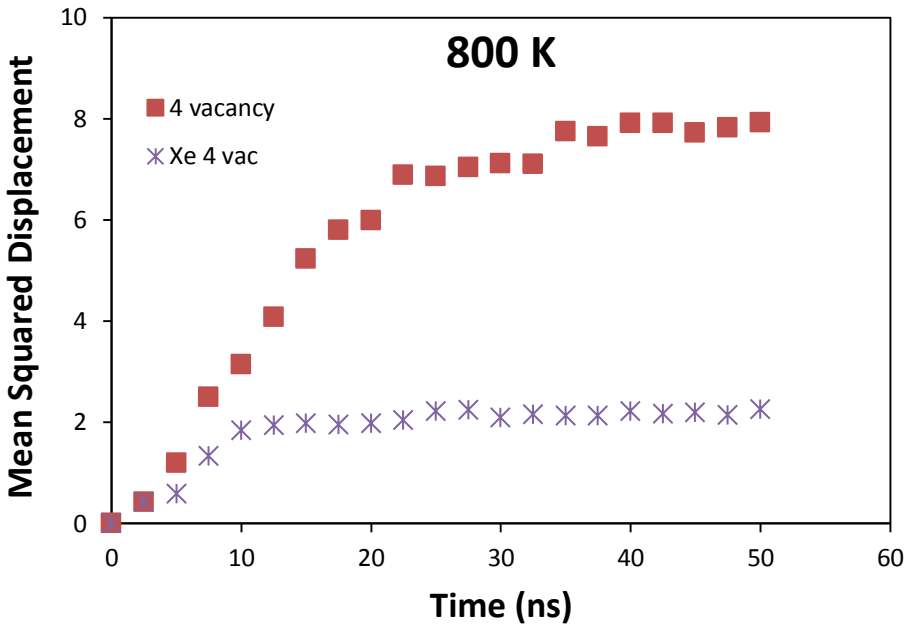


Figure 39. Mean squared displacement of a four vacancy system as a function of time at 800 K. Red squares denote mean square displacement of uranium atoms with four vacancies. Purple asterisks denote mean square displacement of uranium atoms with four vacancies and a xenon substitutional.

Figure 40 displays the msd as a function of time at 900 K for a system containing four vacancies, and a system containing four vacancies with a Xe substitutional. For a system with four vacancies, general linear behavior as a function of time is observed. Opposed to behavior at 800 K, vacancy clustering is not serving to pin vacancies. Clustering is still occurring, however, thermal fluctuations are strong enough to overcome barriers to vacancy diffusion. For the system containing a Xe substitutional, the msd exhibits a plateauing behavior. Thus, vacancies are diffusing through the bulk, finding the Xe atom, clustering and experiencing a pinning effect, limiting further diffusion of the vacancy. Thermal fluctuations are strong enough to overcome vacancy-

vacancy clustering. However, introduction of a Xe substitutional creates a much stronger attractive force and thus a stronger pinning force, inhibiting the diffusion of vacancies.

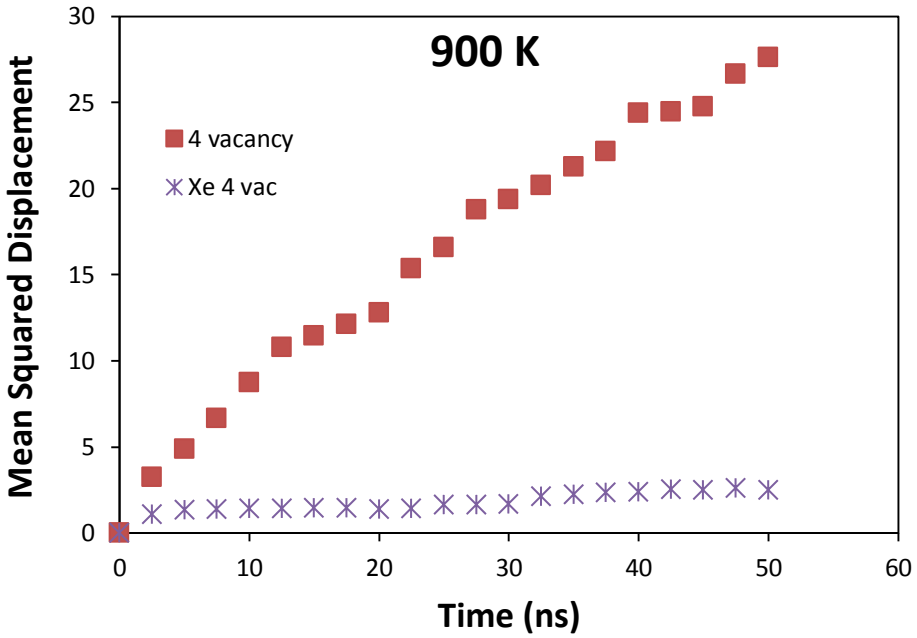


Figure 40. Mean squared displacement of a four vacancy system as a function of time at 900 K. Red squares denote mean square displacement of uranium atoms with four vacancies. Purple asterisks denote mean square displacement of uranium atoms with four vacancies and a xenon substitutional.

Figure 41 displays the msd as a function of time at 1100 K for a system containing four vacancies, and a system containing four vacancies with a Xe substitutional. For a system with four vacancies, general linear behavior as a function of time is observed. Vacancy clustering is still occurring, however, thermal fluctuations are strong enough to overcome barriers to vacancy diffusion, and converged vacancy cluster diffusion is observed. For the system containing a Xe substitutional, the msd exhibits a

plateauing behavior. Thus, vacancies are clustering near the Xe substitutional and experiencing a pinning effect, limiting further diffusion of the vacancy. Thermal fluctuations are strong enough to overcome vacancy-vacancy clustering, but unable to overcome Xe-vacancy binding. Introduction of a Xe substitutional strongly inhibits the diffusion of vacancies. There is in fact a positive slope of the msd as a function of time for the system containing a Xe substitutional. Thus, vacancy diffusion is in fact still occurring and the pinning of vacancies is imperfect. Although vacancy diffusion is in fact still occurring, the amount of diffusion is strongly suppressed due to the presence of a Xe substitutional.

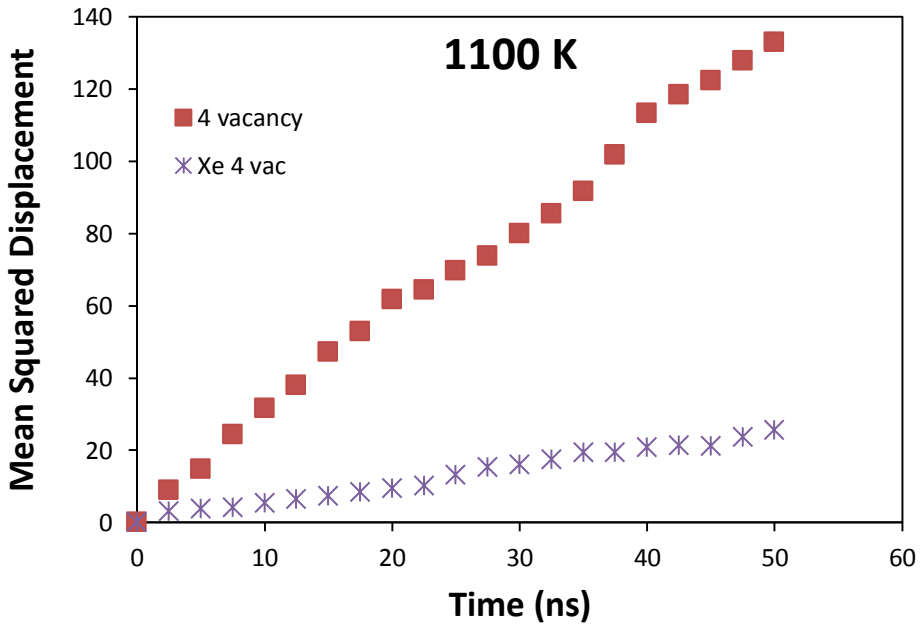


Figure 41. Mean squared displacement of a four vacancy system as a function of time at 1100 K. Red squares denote mean square displacement of uranium atoms with four vacancies. Purple asterisks denote mean square displacement of uranium atoms with four vacancies and a xenon substitutional.

Figure 42 displays the msd as a function of time at 1300 K for a system containing four vacancies, and a system containing four vacancies with a Xe substitutional. For a system with four vacancies, general linear behavior as a function of time is observed. Vacancy clustering is still occurring, and converged vacancy cluster diffusion is observed. For the system containing a Xe substitutional, the msd exhibits a behavior identical to that observed at 1100 K in Figure 41. Limited vacancy diffusion is occurring, and the suppression is due to the presence of a Xe substitutional. In comparison to Figure 41, the msd data points at 1300 K exhibit a more positive slope. Thus, the rate of vacancy diffusion is higher, and thermal fluctuations are more readily able to overcome attractive forces between the Xe substitutional and the vacancies. However, significant depression of diffusion is still occurring due to pinning around the Xe substitutional.

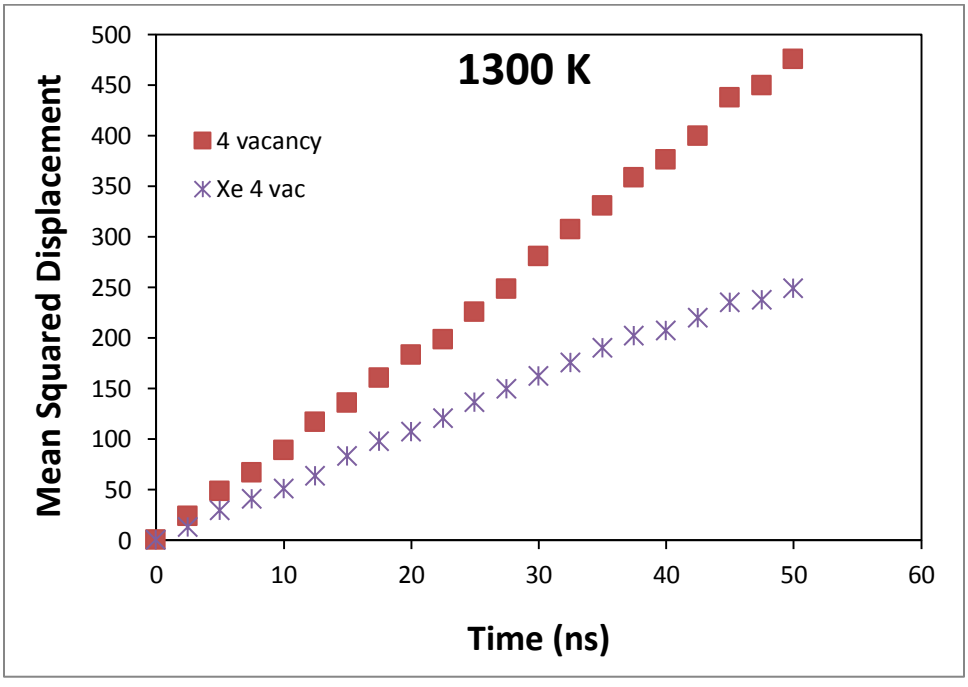

Figure 42. Mean squared displacement of a four vacancy system as a function of time at 1300 K. Red squares denote mean square displacement of uranium atoms with four vacancies. Purple asterisks denote mean square displacement of uranium atoms with four vacancies and a xenon substitutional.

Utilizing the information from mean squared displacement data points as a function of time, diffusion coefficients can be constructed via Einstein's equation:

$$D_{sim} = D = \frac{\langle r^2 \rangle}{6t} \tag{29}$$

where D is the diffusion coefficient, $<r^2>$ is the average mean squared displacement and *t* is the time. This can present us with an estimate of the simulation diffusion coefficient ($D_{sim}$). To account for the inherent bias associated with simulation defect concentrations, $D_{sim}$ can be multiplied by the simulation defect concentration to yield an effective diffusion coefficient:

$$D_{eff} = D_{sim} \times c_v \tag{30}$$

where $c_v$ is the vacancy concentration in the simulation. The effective diffusion coefficient can then be determined as a function of temperature and fit to an Arrhenius equation. The Arrhenius equation has the form of:

$$D = D_0 e^{\left(\frac{-Q}{k_B T}\right)} \tag{31}$$

where $D_0$ is the pre-exponential factor which accounts for geometrical factors and defect concentrations, $k_B$ is the Boltzmann constant and *T* is temperature. The *Q* value is an activation energy. For the diffusion of a single isolated defect in the bulk, *Q* is analogous to the migration barrier. For systems with multiple defects interacting with each other or for systems where a defect interacts with interfaces or other non-bulk entities, the value

of *Q* incorporates information such as binding and energetic attraction. With this in mind, the effective diffusion coefficient for a system with a monovacancy and a system with four vacancies is displayed in Figure 43.

In theory, if all four vacancies were diffusing individually and behaving as monovacancies, the two effective diffusion coefficient curves would be identical. Upon first examination, it is evident that the effective diffusion coefficient for a system with four vacancies is higher than the effective diffusion coefficient for a monovacancy. Also, the migration energy is lower for a four vacancy system (0.7 eV for a four vacancy system, 0.911 eV for a monovacancy). It was mentioned previously that vacancy clustering is in fact occurring in these systems. Given this information, combined with the fact that a multiple vacancy system exhibits a lower migration energy, it becomes clear that vacancy cluster diffusion occurs more rapidly than monovacancy diffusion. Also, whereas it was previously theorized that the majority of self-diffusion in bcc uranium occurs via a monovacancy mechanism, it seems entirely possible that self-diffusion is instead occurring via vacancy clusters.

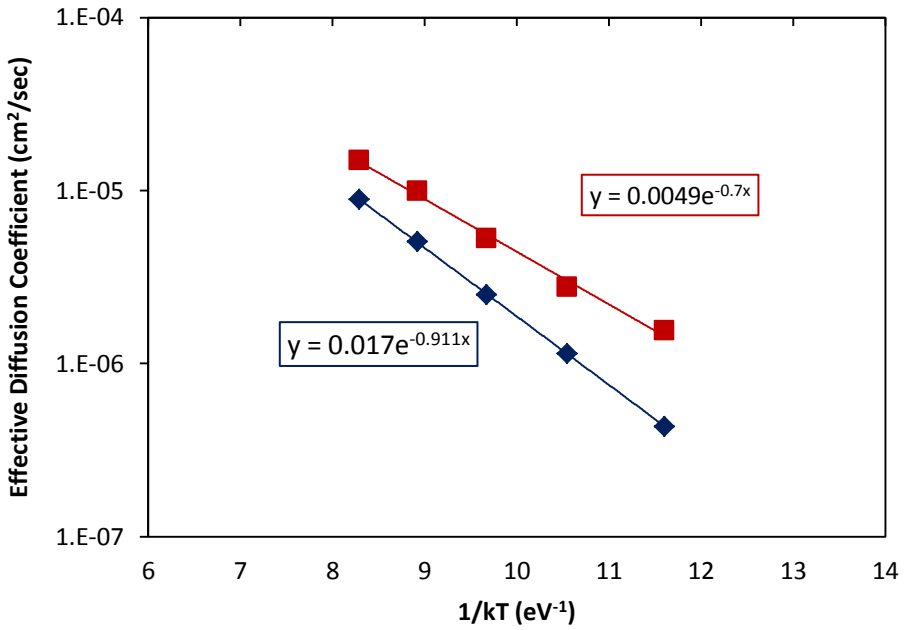


Figure 43. Effective diffusion coefficient as a function of temperature. The monovacancy diffusion coefficient is denoted by blue diamonds. The effective diffusion coefficient for a system with four vacancies is denoted by red squares.

In Figure 44, the effective diffusion coefficient for a system with four vacancies and a system with a Xe substitutional and four vacancies is displayed as a function of temperature. For all temperatures, the effective diffusion coefficient for a system without a Xe substitutional is higher. Thus, it is clearly shown that it is easier for vacancies and vacancy clusters to diffuse in systems with no Xe substitutionals. Also, there is an increase in the *Q* value from 0.7 eV to 1.298 eV corresponding to the introduction of a Xe substitutional in the system. This increase in activation energy is due to the attractive force between Xe substitutionals and vacancies. This attractive force provides an increase in the effective migration barrier for vacancies, and thus an increase in the *Q* value. It is seen that as temperature increases, the difference in the effective diffusion

coefficient between the systems with and without a Xe substitutional is decreased. Thus, the effect of Xe substitutionals acting as pinning sites for vacancies decreases as the temperature increases. However, for all temperatures analyzed, the diffusion of vacancies is suppressed via the presence of a Xe substitutional and vacancy clustering around the Xe substitutional is indeed occurring. Thus, it can be theorized that Xe substitutionals can act as potential nucleation sites for void and bubble formation, due to the inherent attractive forces between the two species.

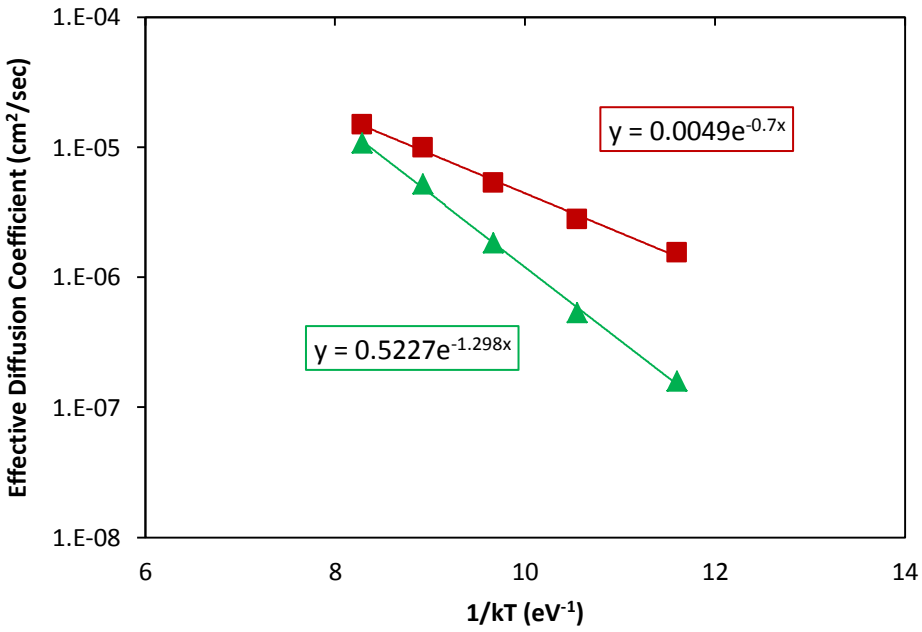


Figure 44. Effective diffusion coefficient of four vacancy systems as a function of temperature. The effective diffusion coefficient for a system with four vacancies is denoted by red squares. The effective diffusion coefficient for a system with a Xe substitutional and four vacancies is denoted by green triangles.

The effective diffusion coefficient for monovacancy systems with and without a Xe substitutional is not graphed within this dissertation. This is due to the fact that in systems above 900 K, the diffusion coefficients of these two systems are identical, and there is no effect on the vacancy mediated self-diffusion from Xe substitutionals, as previously stated.

# CHAPTER 7

# CONCLUSIONS

Previously, there has been a limited amount of research into the calculation of fundamental properties of metallic uranium, particularly related to point defects. In this work DFT calculations were performed using VASP with PAW pseudopotentials. Several important bulk material properties for γ-U are reproduced that agree well with other published results. Calculation of the formation energy for a vacancy was performed in the γ and α allotropes of U. The vacancy formation energy in the α allotrope compares very well with previously published computational work. The vacancy formation energy in the γ allotrope agrees well with previously published computational and experimental work. Formation energies for various interstitial configurations were also calculated, for which there is no experimental data or other calculations to serve as a benchmark. The most likely positions for self-interstitial U atoms in γ-U are the <110> dumbbell, <100> dumbbell, and octahedral interstitials. Self-interstitial atoms are likely to be found in a variety of configurations in α-U. The first comprehensive study for dilute Zr defects in the bcc allotrope of U shows that the substitutional defect is expected to be the prevalent occupation site. The formation energies were calculated for He, Xe, and Kr in various defect configurations in the α and γ phases, for which there is no experimental or computational data to serve as a benchmark. The most likely position for dilute Xe and Kr atoms in γ-U is the substitutional site. Dilute He atoms in γ-U are likely to be found in a wide variety of defect positions due to the comparable formation energies of all defect configurations analyzed. In α-U, He atoms are likely to be found in several different defect locations, while Kr and Xe are likely to be found as substitutionals. In both the α

and γ phases, size effects of fission products appear to dominate, as smaller fission product species generally have lower formation energies. This work was utilized in the construction of modified Embedded-Atom Method interatomic potentials for the bcc phase of uranium as well as the binary systems of U-Xe, U-Kr and U-He. Using this potential, equilibrium volume and elastic constants were calculated at 0 K and found to be in close agreement with previous first principles calculations. Further, the melting point, heat capacity, enthalpy of fusion, thermal expansion and volume change upon melting were calculated and found to be in reasonable agreement with experiment. Calculations of dilute fission gas defects showed reasonable agreement with first principles calculations. Finally, void and xenon bubble energetics were analyzed as a function of temperature. The void formation energy exhibits a power law relationship with respect to the number of vacancies that comprise a given void. The maximum number of xenon atoms that can be incorporated within a bubble before the ejection of a self-interstitial atom is approximately 90% of the number of vacancies constituting the bubble. The effect of Xe substitutionals on vacancy diffusion was analyzed. The presence of Xe substitutionals generally suppresses vacancy diffusion. Increased thermal motion decreases the effect of Xe substitutionals on vacancy diffusion. In multiple vacancy systems, it was seen that Xe substitutionals can serve as potential void and bubble nucleation sites, due to attraction between vacancies and Xe substitutionals. It was shown that vacancy cluster diffusion occurs more rapidly than monovacancy diffusion.

# APPENDIX A: FUTURE WORK

The results presented above represent a significant step towards understanding atomistic processes within metallic nuclear fuel. The results outline numerous basic, but important, material properties that can be utilized in experiments or in other computational methodologies. This work has provided the tools and the framework for further investigations on a wide variety of systems. Further work should include, but not be limited to, molecular dynamics-density functional theory investigations, a study of entropic effects of self-defects and extrinsic defects, organization of vacancy and interstitial clusters, void surface energies, void/bubble-fission gas radius of interaction, fission gas diffusion mechanisms, grain boundary energies and much more. There is a need for experimental investigations for the validation and comparison of this work. Experiments that could be performed include, but are not limited to, resistivity measurements to determine interstitial formation energies, fission gas implantation studies, and tracer diffusion investigations.

# APPENDIX B: SOFTWARE PACKAGES

It should be noted that different software implementations generate different magnitudes for the defect formation energy, while qualitative behavior is consistent. Molecular dynamics investigations of defects, voids and bubbles were performed with LAMMPS [69]. Molecular statics investigations on defects were performed using DYNAMO, a software precursor to LAMMPS.

# REFERENCES


[1] G. Hofman, L. Walter, T. Bauer, Progress in Nucl. Energy, 31 (1997) 83.
[2] W. Carmack, D. Porter, Y. Chang, S. Hayes, M. Meyer, D. Burkes, C. Lee, T. Mizuno, F. Delage, J. Somers, J. Nucl. Mater., 392 (2009) 139.
[3] J. Roberto, T.D. de la Rubia, in: Report of the Basic Energy Sciences Workshop on Basic Research Needs for Advanced Nuclear Energy Systems, 2006.
[4] D.R. Olander, Fundamental Aspects of Nuclear Reactor Elements, ERDA, Springfield, VA, 1975.
[5] L. Leibowitz, R. Blomquist, A. Pelton, J. Nucl. Mater., 167 (1989) 76.
[6] G. Hofman, S. Hayes, M. Petri, J. Nucl. Mater., 227 (1996) 277.
[7] C.S. Yoo, H. Cynn, P. Soderlind, Physical Review B, 57 (1998) 10359-10362.
[8] P. Soderlind, Advances in Physics, 47 (1998) 959-998.
[9] P. Soderlind, Phys. Rev. B, 66 (2002) 085113.
[10] C. Barrett, M. Mueller, R. Hitterman, Phys. Rev. B, 129 (1963) 625.
[11] J. Crocombette, F. Jollet, L. Nga, T. Petit, Phys. Rev. B, 64 (2001) 104107.
[12] C. Taylor, Phys. Rev. B, 77 (2008) 094119.
[13] G. Kresse, J. Furthmuller, Phys. Rev. B, 54 (1996) 11169.
[14] S. Xiang, H. Huang, L. Hsiung, J. Nucl. Mater., 375 (2008) 113.
[15] H. Matter, J. Winter, W. Trifthauser, J. Nucl. Mater., 88 (1980) 273.
[16] G.Y. Huang, B.D. Wirth, J. Phys.: Condens. Matter, 23 (2011) 205402.
[17] J. Sanchez, D. de Fontaine, Phys. Rev. Lett., 35 (1975) 227.
[18] Y. Ye, Y. Chen, K. Ho, B. Harmon, Phys. Rev. Lett., 58 (1987) 1769.
[19] D. Price, B. Cooper, Phys. Rev. B, 39 (1989) 4945.
[20] J. Lennard-Jones, Proc. Phys. Soc., 43 (1931) 461.
[21] M. Baskes, Phys. Rev. B, 62 (2000) 15532.
[22] M. Baskes, Phys. Rev. B, 46 (1992) 2727.
[23] S.M. Valone, M.I. Baskes, Journal of Computer-Aided Materials Design, 14 (2007) 357-365.
[24] A. Kubota, W.G. Wolfer, S.M. Valone, M.I. Baskes, Journal of Computer-Aided Materials Design, 14 (2007) 367-378.
[25] M.I. Baskes, A.C. Lawson, S.M. Valone, Physical Review B, 72 (2005).
[26] M.I. Baskes, S.Y. Hu, S.M. Valone, G.F. Wang, A.C. Lawson, Journal of Computer-Aided Materials Design, 14 (2007) 379-388.
[27] D. Belashchenko, D. Smirnova, O. Ostrovski, High Temp., 48 (2010) 363.
[28] D.E. Smirnova, S.V. Starikov, V.V. Stegailov, J. Phys.: Condens. Matter, 24 (2012) 015702.
[29] Y. Li, T.-R. Shan, T. Liang, S. Sinnott, S. Phillpot, J. Phys.: Condens. Matter, 24 (2012) 235403.
[30] G. Kresse, D. Joubert, Phys. Rev. B, 59 (1999) 1758.
[31] P. Blochl, Phys. Rev. B, 50 (1994) 17953.
[32] P. Blochl, O. Jepsen, O. Anderson, Phys. Rev. B, 49 (1994) 16223.
[33] P. Hohenberg, W. Kohn, Phys. Rev., 136 (1964) B864.
[34] W. Kohn, L. Sham, Phys. Rev., 140 (1965) A1133.
[35] J. Perdew, K. Burke, M. Ernzerhof, Phys. Rev. Lett., 77 (1996) 3865.
[36] J. Perdew, Y. Wang, Phys. Rev. B, 45 (1992) 13244.

[37] M. Methfessel, A. Paxton, Phys. Rev. B, 40 (1989) 3616.
[38] M. Daw, M. Baskes, Phys. Rev. Lett., 50 (1983) 1285.
[39] M. Daw, M. Baskes, Phys. Rev. B, 29 (1984) 6443.
[40] M.S. Daw, S.M. Foiles, M.I. Baskes, Materials Science Reports, 9 (1993) 251-310.
[41] P. Olsson, Comp. Mater. Sci., 47 (2009) 135.
[42] D. Belashchenko, D. Smirnova, Rus. J. Phys. Chem. A, 85 (2011) 1908.
[43] X. Liu, H. Liu, J. Dong, X. Xie, Scripta mater., 42 (1999) 189.
[44] M. Chassange, M. Legros, D. Rodney, Acta Mater., 59 (2011) 1456.
[45] G. Li, Q. Wang, D. Li, X. Lu, J. He, Mater. Chem. Phys., 114 (2009) 746.
[46] I. Vatne, E. Ostby, C. Thaulow, D. Farkas, Mater. Sci. Eng.: A, 528 (2011) 5122.
[47] J. Rose, J. Smith, F. Guinea, J. Ferrante, Phys. Rev. B, 29 (1984) 2963.
[48] M. Baskes, Phys. Rev. Lett., 59 (1987) 2666.
[49] M. Baskes, J. Nelson, A. Wright, Phys. Rev. B, 40 (1989) 6085.
[50] R. Ravelo, M. Baskes, Phys. Rev. Lett., 79 (1997) 2482.
[51] A. Wilson, R. Rundle, Acta Cryst., 2 (1949) 126.
[52] C. Basak, G. Prasad, H. Kamath, N. Prabhu, J. Alloys and Comp., 480 (2009) 857.
[53] C. Yoo, H. Cynn, P. Soderlind, Phys. Rev. B, 57 (1998) 10359.
[54] P. Soderlind, Adv. Phys., 47 (1998) 959.
[55] F. Birch, Phys. Rev., 71 (1847) 809.
[56] M.L. Cohen, Phys. Rev. B, 32 (1985) 7988.
[57] L. Berlu, G. Jomard, G. Rosa, P. Faure, Journal of Nuclear Materials, 372 (2008) 171.
[58] S. Valone, M. Baskes, M. Stan, T. Mitchell, A. Lawson, K. Sickafus, J. Nucl. Mater., 324 (2004) 41.
[59] E. Clementi, D. Raimondi, W. Reinhardt, J. Chem. Phys., 38 (1963) 2686.
[60] P. Nerikar, X.-Y. Liu, B. Uberuaga, C. Stanek, S. Phillpot, S. Sinnott, J. Phys.: Condens. Matter, 21 (2009) 435602.
[61] O. Eriksson, P. Soderlind, J. Willis, A. Boring, Physica B, 190 (1993) 5.
[62] O. Eriksson, J. Willis, P. Soderlind, J. Melsen, R. Ahuja, A. Boring, B. Johansson, J. Alloys and Comp., 213/214 (1994) 268.
[63] G.H. Lander, E.S. Fisher, S.D. Bader, Advances in Physics, 43 (1994) 1-111.
[64] M. Weeks, Discovery of the Elements, Kessinger Publishing Co., Whitefish, MT, 2003.
[65] M. Mendelev, M. Kramer, C. Becker, M. Asta, Philos. Mag., 88 (2008) 1723.
[66] M. Mendelev, Y. Mishin, Phys. Rev. B, 80 (2009) 144111.
[67] M. Mendelev, B. Bokstein, Philos. Mag., 90 (2010) 637-654.
[68] B. Beeler, B. Good, S. Rashkeev, C. Deo, M. Baskes, M. Okuniewski, J. Phys.: Condens. Matter, 22 (2010) 505703.
[69] S. Plimpton, J. Comp. Phys., 117 (1995) 1.